

A gravitationally boosted MUSE survey for emission-line galaxies at $z \gtrsim 5$ behind the massive cluster RCS 0224

Renske Smit,^{1,2,3*} A. M. Swinbank,^{1,4} Richard Massey,^{1,4} Johan Richard,⁵
Ian Smail^{1,4} and J.-P. Kneib^{6,7}

¹Center for Extragalactic Astronomy, Durham University, South Road, Durham DH1 3LE, UK

²Cavendish Laboratory, University of Cambridge, 19 JJ Thomson Avenue, Cambridge CB3 0HE, UK

³Kavli Institute for Cosmology, University of Cambridge, Madingley Road, Cambridge CB3 0HA

⁴Institute for Computational Cosmology, Durham University, South Road, Durham DH1 3LE, UK

⁵Univ Lyon, Univ Lyon1, Ens de Lyon, CNRS, Centre de Recherche Astrophysique de Lyon UMR5574, F-69230, Saint-Genis-Laval, France

⁶Institute of Physics, Laboratory of Astrophysics, Ecole Polytechnique Fédérale de Lausanne (EPFL), Observatoire de Sauverny, 1290 Versoix, Switzerland

⁷Aix Marseille Université, CNRS, LAM (Laboratoire d'Astrophysique de Marseille) UMR 7326, 13388, Marseille, France

Accepted 2017 January 26. Received 2017 January 16; in original form 2016 September 4

ABSTRACT

We present a Very Large Telescope/Multi Unit Spectroscopic Explorer (MUSE) survey of lensed high-redshift galaxies behind the $z = 0.77$ cluster RCS 0224–0002. We study the detailed internal properties of a highly magnified ($\mu \sim 29$) $z = 4.88$ galaxy seen through the cluster. We detect widespread nebular C IV $\lambda\lambda 1548, 1551$ Å emission from this galaxy as well as a bright Ly α halo with a spatially uniform wind and absorption profile across 12 kpc in the image plane. Blueshifted high- and low-ionization interstellar absorption indicate the presence of a high-velocity outflow ($\Delta v \sim 300$ km s^{−1}) from the galaxy. Unlike similar observations of galaxies at $z \sim 2 - 3$, the Ly α emission from the halo emerges close to the systemic velocity – an order of magnitude lower in velocity offset than predicted in ‘shell’-like outflow models. To explain these observations, we favour a model of an outflow with a strong velocity gradient, which changes the effective column density seen by the Ly α photons. We also search for high-redshift Ly α emitters and identify 14 candidates between $z = 4.8 - 6.6$, including an overdensity at $z = 4.88$, of which only one has a detected counterpart in *Hubble Space Telescope*/Advanced Camera for Surveys+Wide Field Camera 3 imaging.

Key words: galaxies: evolution – galaxies: formation – galaxies: high-redshift.

1 INTRODUCTION

Over the last decade, deep observations of blank fields, in particular with the *Hubble Space Telescope* (*HST*) have identified a substantial population of galaxies beyond $z > 3$, using broad-band photometry (e.g. Madau et al. 1996; Steidel et al. 1996, 1999; Sawicki, Lin & Yee 1997; Lehnert & Bremer 2003; Giavalisco et al. 2004; Ouchi et al. 2004; McLure et al. 2009; van der Burg, Hildebrandt & Erben 2010; Bowler et al. 2015; Bouwens et al. 2015a; Finkelstein et al. 2015). Despite the progress in identifying large numbers of galaxies, it remains challenging to obtain spectroscopic redshifts and determine the physical properties of these systems. This is largely due to their inherent faintness and the fact that bright rest-frame optical emission-line tracers such as H α and [O III], which are traditionally used to measure the properties of the interstellar medium (ISM), are shifted to observed mid-infrared wavelengths for sources at $z \gtrsim 3-4$. The small physical sizes of galaxies at

$z > 3$ compared to typical ground-based seeing also makes spatially resolved observations difficult to obtain, inhibiting measurements of dynamical masses, star formation distributions and wind energetics.

Recently, the commissioning of the Multi Unit Spectroscopic Explorer (MUSE) on the Very Large Telescope (VLT) has led to an advance in the identification and characterization of $z \sim 3-6$ galaxies through wide-field and deep spectroscopy of the rest-frame ultraviolet (UV) spectra of these sources. For example, MUSE is starting to probe the physical properties of H II regions within galaxies by exploiting gravitationally lensing through their faint UV nebular emission lines such as C IV $\lambda\lambda 1548, 1551$ Å, He II $\lambda 1640$ Å, O III] $\lambda\lambda 1661, 1666$ Å and C III] $\lambda\lambda 1907, 1909$ Å (Karman et al. 2015; Caminha et al. 2016; Patrício et al. 2016; Vanzella et al. 2016), lines which are rarely seen in local star-forming galaxies (e.g. Hainline et al. 2011; Rigby et al. 2015). These lines are produced either by young, metal-poor stellar populations with high-ionization parameters (e.g. Christensen et al. 2012b; Stark et al. 2014; Rigby et al. 2015; Amorín et al. 2017), or gas photoionization by faint active galactic nuclei (AGN; e.g. Stark et al. 2015; Feltré, Charlot & Gutkin 2016). Furthermore, MUSE has enabled the

* E-mail: RS940@cam.ac.uk

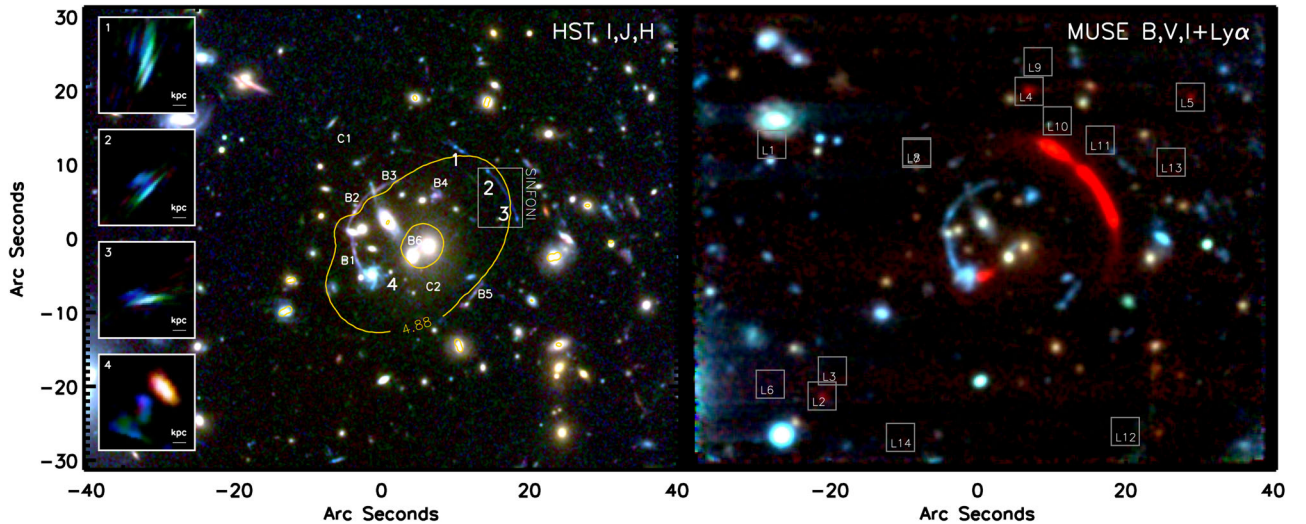


Figure 1. *HST* I_{814} , J_{125} and H_{160} (left-hand panel) and MUSE B , V , $I+7143 \text{ \AA}$ (right-hand panel) colour images of the cluster core of RCS 0224–0002 at $z = 0.77$. The four images of the lensed galaxy at $z = 4.88$ are numbered 1–4 in the left-hand panel and are reconstructed in the source plane in the inset panels. We also indicate the coverage of the SINFONI K -band spectroscopy and the images B1–B6 of a $z_{\text{C III]}} = 2.4$ galaxy and images C1–C2 of a $\text{Ly}\alpha$ emitter at $z_{\text{Ly}\alpha} = 5.5$ that are used as constraints on the lens model (Section 3.1). The $z = 4.8$ – 6.5 $\text{Ly}\alpha$ candidates selected in Section 4 are marked with squares on the right-hand panel (see Section 4 and Appendix D). For the MUSE red channel, we combine a broad-band centred on 6125 \AA with an 8 \AA -wide narrow-band centred on the $\text{Ly}\alpha$ halo around the $z \sim 4.88$ arc (Gladders et al. 2002); the $\text{Ly}\alpha$ emission is clearly extended beyond the continuum. Three sources (L2, L4 and L5) in our blind search for $\text{Ly}\alpha$ emitters (Section 4) are found at the same redshift as the $z = 4.88$ arc, suggesting a galaxy overdensity.

detailed modelling of extended $\text{Ly}\alpha$ emission, gaining insights into the inflowing neutral gas and/or wind energetics in the circumgalactic medium (CGM) of galaxies (Swinbank et al. 2015; Bina et al. 2016; Gullberg et al. 2016; Wisotzki et al. 2016; Vanzella et al. 2017).

Moreover, MUSE is a promising new instrument for undertaking unbiased spectroscopic surveys. Bacon et al. (2015) used a 27 h MUSE pointing of the *HubbleDeepField-South* (HDF-S) to detect 89 $\text{Ly}\alpha$ emitters in the redshift range $z \sim 3$ – 6 . Remarkably, 66 per cent of the $\text{Ly}\alpha$ emitters above $z \gtrsim 5$ have no counterpart in the *HST* broad-band imaging (to a limiting magnitude of $m_i \sim 29.5$),

In this paper, we extend current work on characterizing the UV spectra of intrinsically faint high-redshift galaxies out to $z \sim 5$ through the analysis of VLT/MUSE observations of one of the most strongly magnified galaxies known above a redshift of $z > 3$; the highly magnified ($\mu = 13$ – $145 \times$) $z = 4.88$ lensed arc seen through the core of the compact $z = 0.77$ cluster RCS 0224–0002 (Gladders, Yee & Ellingson 2002; Swinbank et al. 2007, hereafter S07).

S07 observed nebular [O II] emission and an extended $\text{Ly}\alpha$ halo in this $z = 4.88$ source and they hypothesized that a galactic-scale bipolar outflow has recently bursted out of this system and into the intergalactic medium (IGM). Our new observations obtain significantly higher signal-to-noise ratio (S/N) in the UV emission and continuum, allowing us to resolve the shape of the $\text{Ly}\alpha$ profile and detect the UV-ISM lines. Furthermore, our MUSE pointing covers the complete $z \sim 6$ critical curves, which allows for an efficient survey for faint high-redshift $\text{Ly}\alpha$ emitters. These sources are important targets to study in order to understand the properties of the ultra-faint galaxy population that could have contributed significantly to reionization.

This paper is organized as follows: we describe our MUSE data set and we summarize the complementary data presented by S07 in Section 2. We analyse the spectral properties of the main $z = 4.88$ arc in Section 3. We present the results of a blind search for $\text{Ly}\alpha$ emitters in Section 4 and finally we summarize our findings in Section 5.

For ease of comparison with previous studies, we take $H_0 = 70 \text{ km s}^{-1} \text{ Mpc}^{-1}$, $\Omega_m = 0.3$ and $\Omega_\Lambda = 0.7$, resulting in an angular scale of $6.4 \text{ kpc per arcsecond}$ at $z = 4.88$. Magnitudes are quoted in the AB system (Oke & Gunn 1983).

2 DATA

2.1 HST imaging

We obtained *HST* imaging from the Space Telescope Science Institute MAST data archive (GO:14497, PI: Smit and GO: 9135, PI: Gladders). RCS 0224–0002 ($\alpha = 02:24:34.26$, $\delta = -00:02:32.4$) was observed with the Wide Field Planetary Camera 2 (WFPC2) using the $F666W$ (V_{666}) filter (10.5 ks), the Advanced Camera for Surveys (ACS) using the $F814W$ (I_{814}) filter (2.2 ks) and the Wide Field Camera 3 (WFC3) using the $F125W$ (J_{125}) and $F160W$ (H_{160}) filters (2.6 ks each). The ACS and WFC3 images were reduced with DRIZZLEPAC v2.1.3 to 0.05 and $0.128 \text{ arcsec pixel}^{-1}$ resolution, respectively. The depth of the I_{814} , J_{125} and H_{160} band images is 26.3 , 26.8 and 26.7 mag , respectively (5σ in a $0.5 \text{ arcsec-diameter}$ aperture). The WFPC2 data was reduced with the STSDAS package from IRAF to $\sim 0.1 \text{ arcsec pixel}^{-1}$ resolution as described by S07. A false-colour image using the I_{814} , J_{125} and H_{160} bands are shown in Fig. 1. The colour image shows two bright arcs at $z = 2.40$ (lensed images B1–B6) and $z = 4.88$ (lensed images 1–4).

2.2 MUSE spectroscopy

We observed the cluster RCS 0224–0002 with a single pointing ($\sim 1 \text{ arcmin} \times 1 \text{ arcmin}$) of the VLT/MUSE Integral Field Unit (IFU) spectrograph (Bacon et al. 2010) between 2014 November 13 and 2015 September 16, programme 094.A-0141. Each individual exposure was 1500 s , with spatial dithers of $\sim 15 \text{ arcsec}$ to account for cosmic rays and defects. One observing block was partly taken in twilight and therefore omitted from the final data cube, resulting in a co-added exposure time of 13.5 ks . All the observations we use

were taken in dark time with <0.8 arcsec V -band seeing and clear atmospheric conditions.

We reduced the data with the public MUSE ESOREX pipeline version 1.2.1, including bias, dark, flat-fielding, sky subtraction, wavelength and flux calibrations. For each individual exposure, we used the lamp flat-field taken adjacent in time to the observation for illumination correction. The reduced data cubes were registered and stacked using the `EXP_COMBINE` routine. The seeing measured on the combined exposure is ~ 0.68 arcsec full width at half-maximum (FWHM), with a spectral resolution of 94 km s^{-1} (2.2 \AA) FWHM at 7000 \AA .

A false-colour image constructed from the final MUSE cube is shown in Fig. 1. We use median images centred on 5375 \AA , 6125 \AA and 8275 \AA as broad-band inputs and we add an 8 \AA wide mean image centred on 7146 \AA to the red channel to emphasize the $\text{Ly}\alpha$ emission in the $z = 4.88$ arc. All bright *HST* sources are detected in the MUSE continuum, while the $z = 4.88$ arc is clearly detected with spatially extended $\text{Ly}\alpha$ emission. A number of other $\text{Ly}\alpha$ sources are identified at the same redshift (see Section 4).

2.3 SINFONI spectroscopy

To complement the MUSE data set, we exploit the SINFONI IFU spectroscopy presented by S07. Briefly, the SINFONI data were taken in the *HK* grating ($\lambda/\Delta\lambda = 1700$) covering the $[\text{O III}]\lambda\lambda 3726.1, 3728.8 \text{ \AA}$ doublet redshifted to $\sim 2.2 \mu\text{m}$. The $\sim 8 \text{ arcsec} \times 8 \text{ arcsec}$ field-of-view (with a spatial resolution $0.25 \text{ arcsec pixel}^{-1}$) covers the lensed images 2 and 3 of the $z = 4.88$ arc.

3 ANALYSIS AND DISCUSSION

3.1 Lens model

To constrain the intrinsic properties of the emission-line galaxies in this study, we require an accurate lens model. S07 constructed a simple mass-model of RCS 0224–0002 with the two main elliptical galaxies in the centre of the cluster and the dark matter component approximated by single truncated pseudo-isothermal elliptical mass distributions. Their primary observational constraints on the mass configuration are the four lensed images of the $z = 4.88$ arc. However, our MUSE observations also cover the other arcs in the cluster. We extract spectra over the multiply imaged central blue arcs (B1–B6 in Fig. 1) and detect $\text{C III}]\lambda\lambda 1907, 1909 \text{ \AA}$, $\text{O III}]\lambda\lambda 1661, 1666 \text{ \AA}$ emission and $\text{Si II} \lambda 1403 \text{ \AA}$, $\text{Si IV} \lambda\lambda 1394, 1403 \text{ \AA}$, $\text{Si II} \lambda 1526 \text{ \AA}$, $\text{C IV} \lambda\lambda 1548, 1551 \text{ \AA}$, $\text{Fe II} \lambda 1608 \text{ \AA}$, $\text{Al II} \lambda 1671 \text{ \AA}$ absorption in images B1–B6 and measure a redshift $z_{\text{C III]}} = 2.396 \pm 0.001$ from the integrated light of these images (Smit et al., in preparation).

We use these new constraints to update the lens model by S07. As in S07, the lens modelling is performed using the `LENSTOOL` software (Kneib et al. 1996; Jullo et al. 2007; Jullo & Kneib 2009). `LENSTOOL` is a parametric method for modelling galaxy clusters that uses a Markov Chain Monte Carlo (MCMC) fit for a specified number of mass peaks. Each mass peak corresponds to a dark matter halo modelled with a truncated pseudo-isothermal elliptical that is characterized by a position (RA, Dec.), velocity dispersion σ_v , ellipticity ε , truncation radius r_{cut} and core radius r_{core} .

For our updated mass model, we include mass components for the brightest 22 cluster members and two components for the cluster halo. We include constraints from the six images B1–B6 of the $z = 2.396$ galaxy arc, including the de-magnified image in the centre. Another faint arc is identified in the *HST* imaging (D1–D3 in

Table A1), just inside the $z = 4.88$ arc, but we do not detect any emission lines from this source in the MUSE data cube. Furthermore, we search the MUSE cube for bright multiply lensed line emitters and find a $\text{Ly}\alpha$ emitter without an *HST* continuum counterpart at $z_{\text{Ly}\alpha} = 5.500 \pm 0.002$ (labelled C1 at $\alpha = 02:24:34.86$, $\delta = -00:02:16.2$ and C2 at $\alpha = 02:24:34.02$, $\delta = -00:02:36.3$ in Fig. 1). The locations of the $\text{Ly}\alpha$ emitter images are well predicted by the lens model that uses all other constraints and therefore we include this doubly lensed image as an additional constraint. In Fig. 1, we show the critical curve of our new model at a redshift of $z = 4.88$ and we list all multiple images used to constrain the model in Table A1 in Appendix A.

Our mass model differs from that of S07 in three ways. First, owing to the different assumed cosmology, our model is ~ 35 per cent less massive: $M = (3.8 \pm 0.2) \times 10^{14} M_{\odot}$ compared to $M = (5.9 \pm 0.4) \times 10^{14} M_{\odot}$. We recover the S07 mass if we switch back to their cosmology. Secondly, the inclusion of mass from all cluster member galaxies makes the $z = 2.4$ critical line better match the observed features of lensed system B. Thirdly, our distribution of mass is more elongated towards the north-west. The S07 model had close to circular symmetry, forced by a prior on the ellipticity of the cluster-scale dark matter. This resulted in a scatter of $\text{rms}_i^A = 1.21$ arcsec between the predicted and observed positions of images A1–A4 (Smith et al., private communication). By dropping the prior (and simultaneously imposing constraints from newly identified lens systems), a cluster-scale mass distribution with ellipticity $\varepsilon = 0.63$ achieves $\text{rms}_i^A = 0.52$ arcsec, or $\text{rms}_i = 1.03$ arcsec for all image systems. However, we achieve a still-better fit ($\text{rms}_i^A = 0.48$ arcsec, $\text{rms}_i = 0.88$ arcsec) using two cluster-scale haloes. These were given a Gaussian prior centred on the two BCGs. The first gets asymmetrically offset to the north-west; the second remains near CG2. This two-halo model achieves a superior $\log(\text{Likelihood})$ of -26.57 and $\chi^2 = 61.3$ in 11 degrees of freedom compared to the best-fitting one-halo model, which has $\log(\text{Likelihood})$ of -142.92 and $\chi^2 = 294$ in 17 degrees of freedom. The best-fitting parameters are listed in Table A2 in Appendix A.

3.2 The $z = 4.88$ arc

The $z = 4.88$ arc was first discovered in the Red-Sequence Cluster (RCS) by Gladders et al. (2002). Gladders et al. (2002) detected the bright $\text{Ly}\alpha$ emission in galaxy images 1–3 at $z_{\text{Ly}\alpha} = 4.8786$ with VLT/FORS-2 spectroscopy. S07 targeted the arc with VLT/VIMOS (galaxy images 1–4) and VLT/SINFONI (galaxy images 2–3) spectroscopy and detected $\text{Ly}\alpha$ at $z_{\text{Ly}\alpha} = 4.8760$ and $[\text{O II}]\lambda\lambda 3726.1, 3728.8 \text{ \AA}$ at $z_{[\text{O II}]}} = 4.8757$. S07 measured a star formation rate of $12 \pm 2 M_{\odot} \text{ yr}^{-1}$, a velocity gradient of $\lesssim 60 \text{ km s}^{-1}$ and an estimated dynamical mass of $\sim 10^{10} M_{\odot}$ within 2 kpc from the $[\text{O II}]$ emission lines.

For our MUSE study of the $z = 4.88$ arc, we will assume that the systemic velocity of the galaxy is best estimated by $z_{\text{sys}} = z_{[\text{O II}]} = 4.8757 \pm 0.0005$ (integrated over galaxy images 2–3). Furthermore, from our lens model, we find luminosity-weighted amplifications of $\mu = 29_{-11}^{+9}$, $\mu = 21_{-8}^{+12}$, $\mu = 138_{-74}^{+7}$ and $\mu = 1.30_{-0.01}^{+0.01}$ for images 1, 2, 3 and 4, respectively (note that image 3 has a very high amplification, but also a very large uncertainty, because the arc crosses the critical curve). These values are slightly higher than the mean, luminosity-weighted magnification of $\mu = 16 \pm 2$ found by S07 for images 1, 2 and 3 integrated (though within the uncertainties for images 1 and 2). The uncertainty on our numbers is largely due to the fact that a small shift of the critical curve can change the luminosity-weighted amplification significantly. In particular,

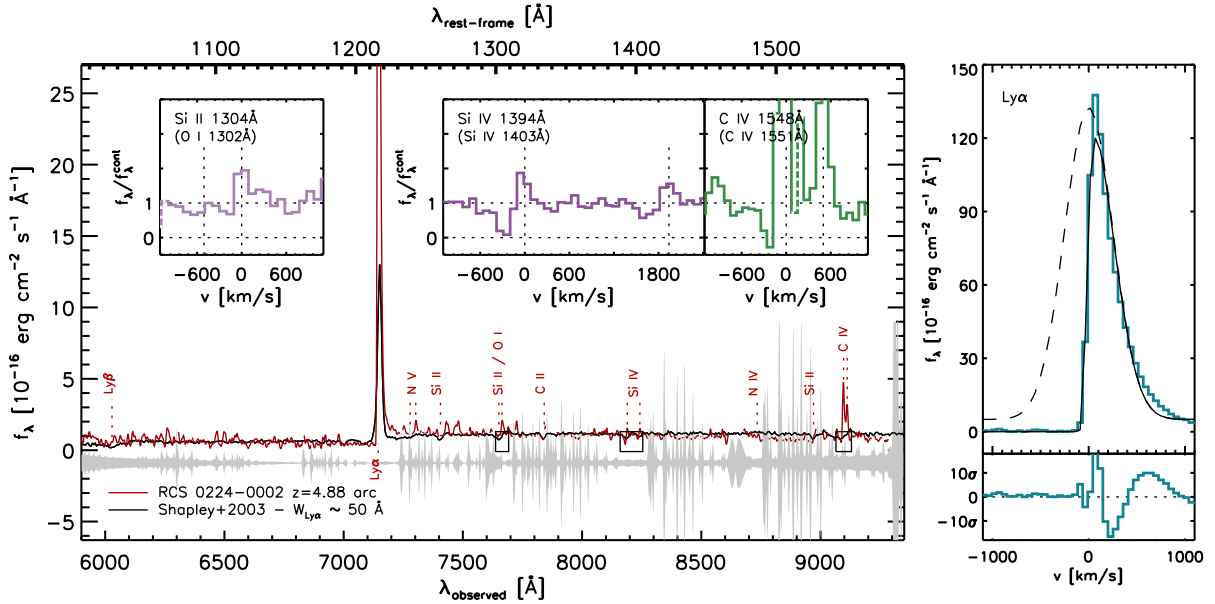


Figure 2. Left-hand panel: the MUSE one-dimensional spectrum extracted over the stellar continuum of the $z = 4.88$ arc (red line), smoothed with a Gaussian filter with $\sigma = 3 \text{ \AA}$ (the grey filled region shows the sky spectrum, offset from the spectrum for clarity). Regions with strong sky emission lines are omitted for clarity. The solid black line indicates the stacked spectrum of the strongest Ly α emitting Lyman break galaxies in the Shapley et al. (2003) sample. The spectrum is normalized to match the $z = 4.88$ arc continuum at $\sim 7500 \text{ \AA}$ and redshifted to $z_{[\text{O II}]} = 4.8757$. The inset panels show the spectra with respect to the [O II] redshift for the Si II $\lambda 1304 \text{ \AA}$, Si IV $\lambda 1394 \text{ \AA}$ and C IV $\lambda 1548 \text{ \AA}$ lines (indicated with black squares on the main spectrum). The spectra are binned to two times lower spectral sampling (2.5 \AA pix^{-1}) and the position of the O I $\lambda 1302 \text{ \AA}$, Si II $\lambda 1304 \text{ \AA}$, Si IV $\lambda \lambda 1394, 1403 \text{ \AA}$ and C IV $\lambda \lambda 1548, 1551 \text{ \AA}$ lines are indicated with dashed lines. The parts of the spectra strongly affected by skylines are indicated with a dashed line in the insets. We detect a single-peaked, strongly asymmetric Ly α line, narrow and strong C IV emission and narrow blueshifted C IV and Si IV absorption lines. All absorption features are significantly blueshifted with respect to the [O II] redshift. Right-hand panel: zoom-in of the observed Ly α line (blue line, top panel) and a Gaussian with Voigt-profile absorber fit to the data (black lines). The narrow Ly α peak in combination with the high-velocity tail are not well described by this simple model as shown by the residuals (bottom panel).

we note that the high magnification of image 3 is dominated by a few pixels that overlap with the critical curve, while the estimated magnification for any modelling method is most uncertain near the critical curves (see Meneghetti et al. 2016).

To measure the detailed properties of the UV spectrum of this galaxy, we first construct a one-dimensional spectrum (up to $\sim 1600 \text{ \AA}$ in the rest frame) of the $z = 4.88$ arc from the MUSE cube by measuring the integrated (non-weighted) spectrum extracted from pixels in the lensed images 1, 2 and 3 with an $S/N > 2\sigma$ in the continuum image of the MUSE data cube. The resulting spectrum is shown in Fig. 2. As well as bright Ly α emission, which has an observed equivalent width (EW) of $793 \pm 159 \text{ \AA}$ (rest-frame $\text{EW}_0 = 135 \pm 27 \text{ \AA}$); we clearly detect the absorption-line doublet Si IV $\lambda \lambda 1394, 1403 \text{ \AA}$, which originates in the ISM and/or CGM and the emission-line doublet C IV $\lambda \lambda 1548, 1551 \text{ \AA}$, with some evidence for an absorption component as well (see inset panels), which is likely to arise from a combination of stellar, nebular and ISM/CGM components. The observational parameters of the UV spectroscopic features in the MUSE data are listed in Table 1 (see Appendix B for measurements on the individual lensed galaxy images).

In the next sections, we will first discuss the morphology of the emission lines, before moving to a detailed analysis of the spectral properties of the $z = 4.88$ arc, the kinematics of the system and the physical picture that emerges from these observations.

3.2.1 Ly α morphology

The Ly α emission in the $z = 4.88$ arc (see Fig. 1) appears to be significantly extended. Lyman break galaxies and Ly α emitters at $z \sim 2-6$

Table 1. Detected spectral features of the $z = 4.88$ arc (integrated over galaxy images 1, 2 and 3).

Line	z	$\Delta v \text{ (km s}^{-1}\text{)}^a$	$\text{EW}_0 \text{ (\AA)}$
Emission lines			
Ly α^{halo}	4.8770 ± 0.0005^b	68 ± 37	278 ± 55
Ly α^{cont}	4.8770 ± 0.0005^b	68 ± 37	135 ± 27
Si II $\lambda 1304 \text{ \AA}$	4.8761 ± 0.0006	21 ± 41	1.1 ± 0.1
Si IV $\lambda 1394 \text{ \AA}$	4.8738 ± 0.0003	-96 ± 29	0.6 ± 0.1
Si IV $\lambda 1403 \text{ \AA}$	4.8752 ± 0.0006	-27 ± 39	0.6 ± 0.1
C IV $\lambda 1548 \text{ \AA}$	4.8753 ± 0.0001	-23 ± 26	5.6 ± 0.4
C IV $\lambda 1551 \text{ \AA}$	4.8755 ± 0.0001	-12 ± 26	3.7 ± 0.3
Absorption lines			
Si II $\lambda 1304 \text{ \AA}^c$	4.8710 ± 0.0001	-240 ± 25	-0.2 ± 0.1
Si IV $\lambda 1394 \text{ \AA}$	4.8694 ± 0.0001	-322 ± 26	-1.1 ± 0.1
Si IV $\lambda 1403 \text{ \AA}$	4.8693 ± 0.0002	-327 ± 28	-0.5 ± 0.1
C IV $\lambda 1548 \text{ \AA}$	4.8694 ± 0.0001	-322 ± 26	-0.8 ± 0.1

^aVelocity offset with respect to the systemic redshift $z_{[\text{O II}]} = 4.8757 \pm 0.0005$. Uncertainties combine the uncertainty on the line redshift with the uncertainty on the [O II] redshift. ^bUsing the peak of the Ly α line. ^cBlended with the O I $\lambda 1302 \text{ \AA}$ line.

often exhibit extended Ly α haloes around the stellar continuum of the galaxies, following an exponential surface-brightness distribution (Steidel et al. 2011; Matsuda et al. 2012; Momose et al. 2014; Wisotzki et al. 2016). These Ly α haloes are thought to be generated either by cooling radiation (e.g. Dijkstra, Haiman & Spaans 2006; Dijkstra & Loeb 2009; Faucher-Giguère et al. 2010; Rosdahl & Blaizot 2012) or by resonant scattering from a central powering

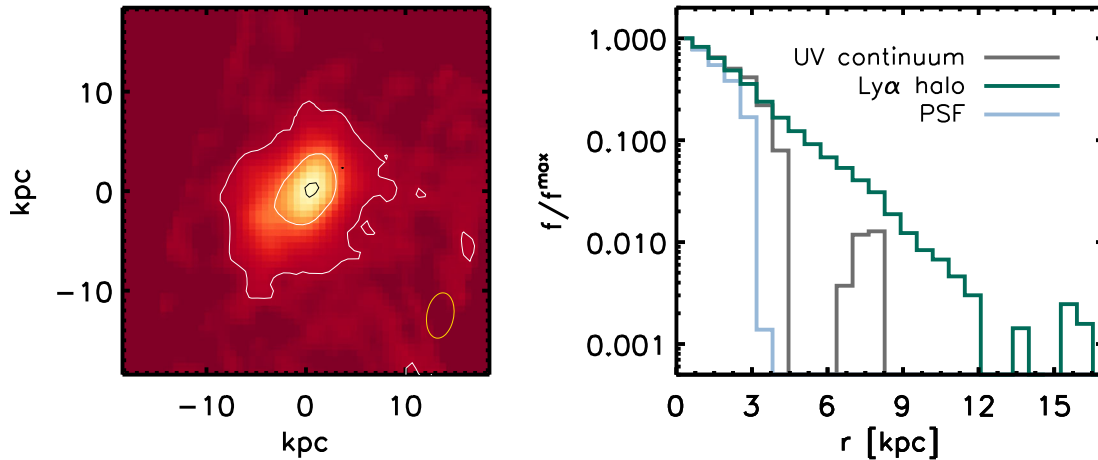


Figure 3. Left: the source-plane reconstruction of the Ly α halo of the lensed galaxy image 4. White contours indicate 50 per cent and 10 per cent of the peak flux in the Ly α halo, while the yellow ellipse in the corner indicates the 50 per cent peak flux for the de-lensed PSF of the MUSE continuum image. The black contour indicates 50 per cent of the peak flux of the UV continuum observed in the *HST* I_{814} band. The Ly α flux is dominated by a smooth and largely circularly symmetric halo that is extended beyond the stellar continuum, but we also identify an extended region to the south-east (north-west in the image plane). Right: the exponential surface-brightness profile of the Ly α halo, compared to the MUSE continuum (using a foreground-subtracted broad-band image at 7400 Å) surface-brightness profile and the MUSE PSF measured from the source-plane reconstruction of galaxy image 4. The Ly α halo is extended beyond the stellar component measured from the UV continuum.

source, such as star formation or AGN (e.g. Verhamme, Schaerer & Maselli 2006; Gronke, Bull & Dijkstra 2015). First, we investigate the morphology of Ly α in the $z = 4.88$ arc behind RCS 0224–0002.

Fig. 3 shows the source-plane reconstruction of the continuum-subtracted Ly α halo. We use image 4, since the Ly α haloes of images 1–3 are incomplete and merged together (see the right-hand panel of Fig. 1). For the spatial profile, we use bins of 0.1 arcsec in concentric circles around the peak flux of the Ly α emission. The MUSE Ly α halo has an observed FWHM of 2.2 kpc, while the *HST* continuum has an FWHM of 0.2 kpc. A number of foreground cluster galaxies contaminate the measurement of the stellar spatial profile directly from the continuum image. Therefore, we construct a broad-band image redwards of Ly α , centred on 7400 Å, and we subtract a continuum image bluewards of the Ly α break centred on 6975 Å in order to remove most of the foreground contamination. We mask any remaining flux from foreground sources by hand. Furthermore, we extract the point spread function (PSF) from a nearby star and place this at the position of the Ly α peak in our lens model in order to construct the source-plane image of the PSF and measure its spatial profile.

The Ly α halo appears roughly isotropic, with little substructure, except for an extended lower luminosity region in the south-east. Comparing the Ly α halo with the UV continuum image in Fig. 3 indicates the extended nature of the faint Ly α profile beyond the continuum. The Ly α halo is consistent with an exponential profile. For comparison with Ly α haloes in the literature, we measure the Petrosian radius (Petrosian 1976) of the halo, defined as the annulus where the Ly α flux is equal to η times the mean flux within the annulus. The Petrosian radius is a useful measure, since it is only weakly dependent on the seeing of the observations. For $\eta = 20$ per cent, we find $R_{p20, Ly\alpha} = 8.1 \pm 0.4$ kpc and $R_{p20, UV} = 2.9 \pm 0.8$ kpc, which is somewhat lower than the range of Petrosian radii $R_{p20, Ly\alpha} \sim 10$ –30 kpc (for $R_{p20, UV} \sim 1.3$ –3.5 kpc) found by Wisotzki et al. (2016), but similar to some of the largest Ly α haloes around $z \sim 0$ analogues in the LARS sample (Hayes et al. 2013), which typically show radii $R_{p20, Ly\alpha} \lesssim 8$ kpc (Fig. 4).

Faucher-Giguère et al. (2010) and Rosdahl & Blaizot (2012) use radiative transfer simulations to investigate the expected

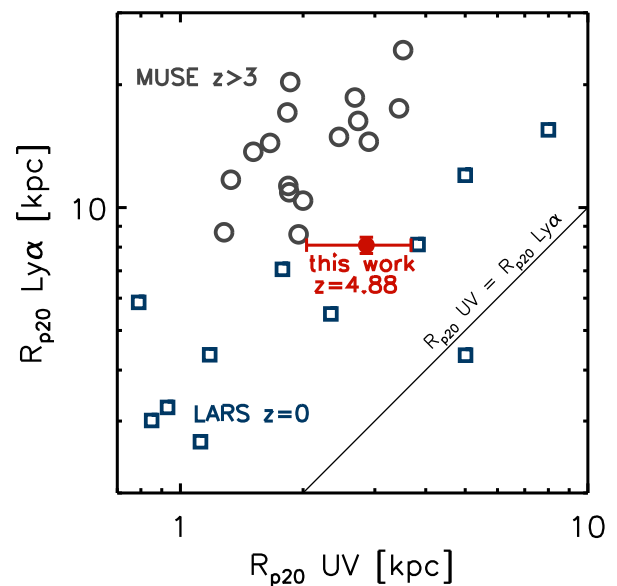


Figure 4. A comparison of the Ly α and UV continuum Petrosian scale radii for the $z = 4.88$ arc and including measurements at $z = 0$ –6 from the Ly α reference sample (LARS; Hayes et al. 2013) and MUSE HDF-S observations (Wisotzki et al. 2016).

morphology of Ly α haloes generated by cooling radiation and they predict concentrated emission, which can extend out to 10–30 kpc. While stacked Ly α haloes extend out to ~ 100 kpc (Steidel et al. 2011; Matsuda et al. 2012; Momose et al. 2014), indicating cooling is not the origin of Ly α emission in typical galaxies, our observations do not have sufficient S/N to trace the $z = 4.88$ Ly α halo beyond 10 kpc, necessary to rule out a gas-cooling scenario. We will therefore further investigate whether the faint, extended Ly α emission is produced by resonant scattering from a central source or by cooling radiation in Section 3.2.2 based on the spectral properties of the line.

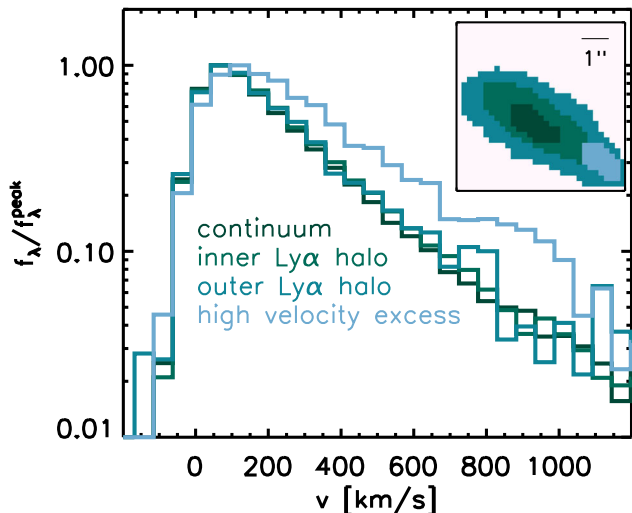


Figure 5. The spatial dependence of the Ly α velocity profile (with respect to the [O II] redshift) in different bins in the image plane of galaxy image 1. The black line indicates the flux within a contour over the stellar continuum flux and the green lines are emitted within contours of constant Ly α flux. The light blue line indicates a region of high-velocity excess flux. The pixels used to generate the four spectra are shown in the inset panel. The spatial variation of the Ly α halo is surprisingly small, with the peak of the Ly α line varying less than the width of one spectral element corresponding to $\sim 60 \text{ km s}^{-1}$. The small difference in the velocity profile between the inner and outer halo would suggest that the bulk of the Ly α photons are CGM generated/rescattered, since there is no evidence for an ISM component that falls away as we observe Ly α further away from the stellar continuum. Spatially offset from the spherical halo, we detect excess flux out to 1000 km s^{-1} (corresponding to the extended region to the south-east in the source-plane image shown in Fig. 3), possibly indicating a collimated high-velocity outflow superimposed on an isotropic component that dominates the total Ly α emission (see Section 3.2.1).

3.2.2 Spectral properties of the Ly α line

High-redshift Ly α emitters can exhibit a wide range of spectral properties, such as blueshifted and redshifted emission, single- and double-peaked lines and different linewidths and velocity offsets, which gives insight into the emission mechanism of Ly α and the column density and velocity distribution of the ISM and CGM neutral gas (e.g. Verhamme et al. 2006; Gronke et al. 2015).

For the $z = 4.88$ arc, the Ly α emission-line profile is very asymmetric and we find a single redshifted Ly α line, with a peak at $z_{\text{Ly}\alpha} = 4.8770 \pm 0.0005$ (using the wavelength and width of the spectral element where Ly α peaks), $\sim 40\text{--}90 \text{ km s}^{-1}$ redshifted with respect to the [O II] emission that marks the systemic redshift, and $\text{FWHM}_{\text{red}} = 285 \text{ km s}^{-1}$, with very little flux bluewards of the [O II] redshift (see Figs 2 and 5). We set an upper limit on the presence of a weaker blue line; at $-\nu_{\text{red}}$, we find an upper limit on the flux ratio of any blue peak to the red peak $F_{\text{peak, blue}}/F_{\text{peak, red}} < 0.027$. Furthermore, we detect a faint tail of redshifted Ly α emission out to $\sim 1000 \text{ km s}^{-1}$. A simplified model for this asymmetric line shape is that of a Gaussian emission-line profile convolved with a Voigt profile, describing the collisional and Doppler broadening of interstellar absorption lines, as shown in Fig. 2, where we fix the redshift of the underlying Gaussian emission to the [O II] redshift $z = 4.8757$. The best-fitting model in Fig. 2 indicates an H I absorber with a column density of 10^{19} cm^{-2} ; however, the fit fails to reproduce both the narrow peak and the high-velocity tail of the Ly α line. In fact, the emission-line component of the Ly α line shows

a strongly non-Gaussian shape; instead we observe an exponential profile as a function of velocity over two orders of magnitude in flux (Fig. 5), remarkably similar to the exponential surface-brightness profile (Fig. 3).

S07 observed the modest redshifted narrow Ly α line in combination with the high-velocity tail, and interpreted this as a combination of emission from the central source combined with redshifted emission from an outflow. To test this model, in Fig. 5, we show the spatial variation of the spectral Ly α profile in the image plane of the lensed galaxy image 1 (the highest S/N image). While we used the source-plane reconstruction of galaxy image 4 for deriving the spatial properties of the Ly α halo, we use the brightest galaxy image for spectral analysis to obtain higher S/N information. First, we partition the halo along contours of constant observed Ly α flux. While the Ly α flux in the halo drops by more than an order of magnitude compared to the emission over the stellar continuum, the shape of the Ly α profile, after normalizing to the peak flux, changes only marginally from the Ly α profile extracted over the stellar continuum. Across the lensed image, the wavelength of the peak of the Ly α line changes by less than $\sim 50 \text{ km s}^{-1}$, while the width and the shape of the high-velocity tail stay nearly constant (see also Patrício et al. 2016, for a similar pattern in a Ly α halo at $z = 3.51$).

These results differ strongly from the scenario described in S07, where the main peak of the Ly α profile comes directly from the star-forming regions and the high-velocity wing is re-scattered in an expanding shell of gas within the CGM. For this model to hold, we would expect the star formation component (the peak of Ly α) to drop off rapidly with increasing radius, while the back-scattered CGM component changes little with radius, and therefore the peak flux would shift to higher velocities and the shape would change significantly. The spatially uniform Ly α spectral profile instead suggests that the Ly α peak is also produced or resonantly scattered within the CGM, which generates Ly α emission with a wide range in velocities.

We can test this further by searching for any deviations from the average Ly α profile. We use the spectrum extracted over the stellar continuum as a model for fitting the Ly α line in each individual pixel of the $z = 4.88$ arc, leaving the normalization as the only free parameter and considering only the peak of the Ly α line as a model constraint. After subtracting our one-parameter model, we detect only a weak residual. In Fig. 5, we show the spectrum extracted over the region with the largest residual, which shows a slightly offset peak compared to the Ly α extracted over the stellar continuum and a broadened profile out to 1000 km s^{-1} , indicating a collimated high-velocity outflow on top of the isotropic Ly α halo component that is described above.

Given the extended nature of the Ly α emission (Section 3.2.1), we now consider various generation mechanisms for the emission. Given the spatially invariant Ly α line profile, which indicates that only a minor fraction of the Ly α emission reaches us directly from the galaxy, it is reasonable to consider whether the halo can be produced by cooling radiation from the CGM. Dijkstra et al. (2006) and Faucher-Giguère et al. (2010) model such scenarios using radiative transfer simulations and find that Ly α should typically be double peaked and blueshifted with respect to the systemic velocity of the galaxy. Assuming that these models provide a reasonable description of the system, the single-redshifted Ly α peak that we observe excludes cooling as a source of Ly α photons in the $z = 4.88$ arc.

To reproduce the Ly α line profile for the $z = 4.88$ arc, we thus favour a picture where a central powering source is surrounded by a largely isotropic halo of neutral gas, which dampens Ly α bluewards of the systemic velocity and resonantly scatters the vast majority of

photons towards higher velocities within the expanding gas behind the galaxy (e.g. Dijkstra et al. 2006; Verhamme et al. 2006).

The strong similarity between the Ly α surface-brightness profile (Fig. 3) and the spectral profile in the $z = 4.88$ arc could suggest the presence of a smoothly varying velocity gradient in the CGM gas that resonantly scatters the Ly α photons into our line of sight. This scenario is qualitatively in good agreement with the Ly α profile considered in Verhamme et al. (2006, see their fig. 7), shown in Appendix C, where the relatively low column density (at a given velocity) created by the strong velocity gradient causes the escape of Ly α photons predominantly at low velocity (and small radii), while a weak high-velocity tail is still observed due to the photons that are resonantly scattered through the accelerating outflow. A model with a gas velocity gradient furthermore predicts the absence of a blue peak, which is difficult to reproduce in a shell model, since a low-velocity shell with low covering fraction that gives rise to a red Ly α peak close to the systemic velocity also produces a nearly symmetric blue peak. In Section 3.3, we will discuss how this model fits into a physical picture that can explain our full set of observations.

3.2.3 C IV emission

The detection of narrow (FWHM = 156 ± 16 km s $^{-1}$) C IV $\lambda\lambda 1548, 1551$ Å emission in the $z = 4.88$ arc is interesting since the UV spectra of field galaxies generally show C IV in absorption from ISM/CGM gas, or else exhibit a P-Cygni profile from the stellar winds of O-stars, with C IV emission redshifted by a few hundred km s $^{-1}$ (Leitherer et al. 2001; Shapley et al. 2003; Jones, Stark & Ellis 2012). AGN can also produce C IV in emission, though with typical linewidths of at least a few hundred km s $^{-1}$. Narrow C IV $\lambda\lambda 1548, 1551$ Å has so far been observed in a handful of strongly lensed high-redshift galaxies (e.g. Holden et al. 2001; Christensen et al. 2012b; Stark et al. 2014, 2015; Caminha et al. 2016; Vanzella et al. 2016). To date these galaxies have either been studied with slit spectroscopy or they are unresolved in ground-based observations, inhibiting the study of the spatial distribution of the C IV $\lambda\lambda 1548, 1551$ Å. The MUSE observations of the brightly lensed $z = 4.88$ arc therefore provides us with a unique opportunity to investigate the origin of this line in more detail.

In the absence of rest-frame optical spectroscopy, a common approach to assessing the possible presence of AGN is using UV emission-line ratios (e.g. Stark et al. 2015; Feltre et al. 2016). At $z = 4.88$, this requires near-infrared spectroscopy to measure the He II $\lambda 1640$ Å and C III] $\lambda\lambda 1907, 1909$ Å lines. With the current observations, we can only assess the C IV/Ly α ratio, which has a ratio of $\gtrsim 0.2$ in the composite spectra of AGN (Shapley et al. 2003; Hainline et al. 2011). In contrast, this ratio is C IV/Ly $\alpha = 0.054 \pm 0.006$ in the $z = 4.88$ arc, with little variation along the images, consistent with the interpretation that this line is associated with star formation and not with a hidden AGN. Fig. 6 shows the C IV/Ly α ratio as a function of Ly α EW for various lensed galaxies in the literature (Christensen et al. 2012b; Stark et al. 2014, 2015; Caminha et al. 2016; Vanzella et al. 2016) and in five spatial bins along the lensed image 1 of the $z = 4.88$ arc (using both the 1548 and 1551 Å lines). The C IV/Ly α ratio and the observed EW of C IV 55 ± 2 Å (rest-frame EW $_0 = 9.3 \pm 0.4$ Å) do not change significantly as a function of position along galaxy image 1. Furthermore, we observe no strong emission from typical AGN lines such as N V $\lambda 1240$ Å, S IV $\lambda\lambda 1393, 1402$ Å and N IV $\lambda\lambda 1483, 1486$ Å (e.g. Hainline et al. 2011).

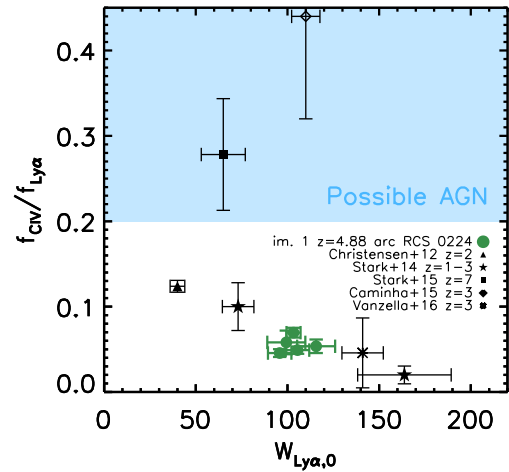


Figure 6. Comparison of the emission-line ratio C IV/Ly α as a function of rest-frame Ly α EW with similar detections in the literature. We show the measurements along the lensed image 1 of the $z = 4.88$ arc. We also show data from lensed C IV emitters at $z \sim 2$ found by Christensen et al. (2012b), Stark et al. (2014), Stark et al. (2015), Caminha et al. (2016) and Vanzella et al. (2016). Narrow-line AGN has been observed to show an emission-line ratio of C IV/Ly $\alpha \gtrsim 0.2$ (Shapley et al. 2003; Erb et al. 2010; Hainline et al. 2011). Along the $z = 4.88$ arc, this emission-line ratio is steady and always below C IV/Ly $\alpha < 0.1$ (see Section 3.2.3).

In Fig. 7, we show the spatial distribution of C IV $\lambda\lambda 1548, 1551$ Å, using a continuum-subtracted narrow-band image of the C IV emission and overlaying the contours on the *HST* continuum image. C IV clearly extends along the arc and shows a morphology that is consistent with the [O II] emission. While we would expect a centrally concentrated source for C IV, if it was originating from an AGN, we can distinguish at least four different ‘clumps’ in the C IV morphology with similar brightness, suggesting that the C IV emission is nebular in origin and emerging from multiple star-forming regions throughout the galaxy.

Finally, we measure the UV-continuum slope β ($f_\lambda \propto \lambda^\beta$) from the $J_{125} - H_{160}$ colour of galaxy image 1 (integrated flux) and find $\beta = -2.19 \pm 0.14$, while the individual star-forming clumps along the arc show slopes between $\beta = -1.68 - -2.64$. Since high-redshift galaxies that host faint AGN have measured UV continuum slopes of $\beta \sim -1.4 - -0.3$ (Hainline et al. 2011; Giallongo et al. 2015) and we therefore conclude that low-mass accreting black holes are unlikely to contribute to the radiation field giving rise to the C IV emission.

3.2.4 Metal-absorption lines

The high-ionization C IV $\lambda\lambda 1548, 1551$ Å line is expected to be a combination of nebular, stellar and ISM/CGM components. While no absorption by the ISM appears present at the systemic velocity of C IV, blueshifted C IV absorption is observed at $\Delta v = -322 \pm 26$ km s $^{-1}$, which also has a narrow profile, with FWHM ~ 200 km s $^{-1}$.

The spectrum displays a strong similarity between the C IV $\lambda 1548$ Å and Si IV $\lambda 1394$ Å absorption profiles (Fig. 2), indicating that the absorption of both lines is due to highly ionized gas clouds in the ISM/CGM of the galaxy moving towards us. Furthermore, both Si IV $\lambda 1394$ Å and Si II $\lambda 1304$ Å show no evidence for absorption at the systemic velocity (Fig. 2) and we even find weak emission lines, possibly indicating a low covering fraction of gas in the ISM of the galaxy. Given the strong absorption of the

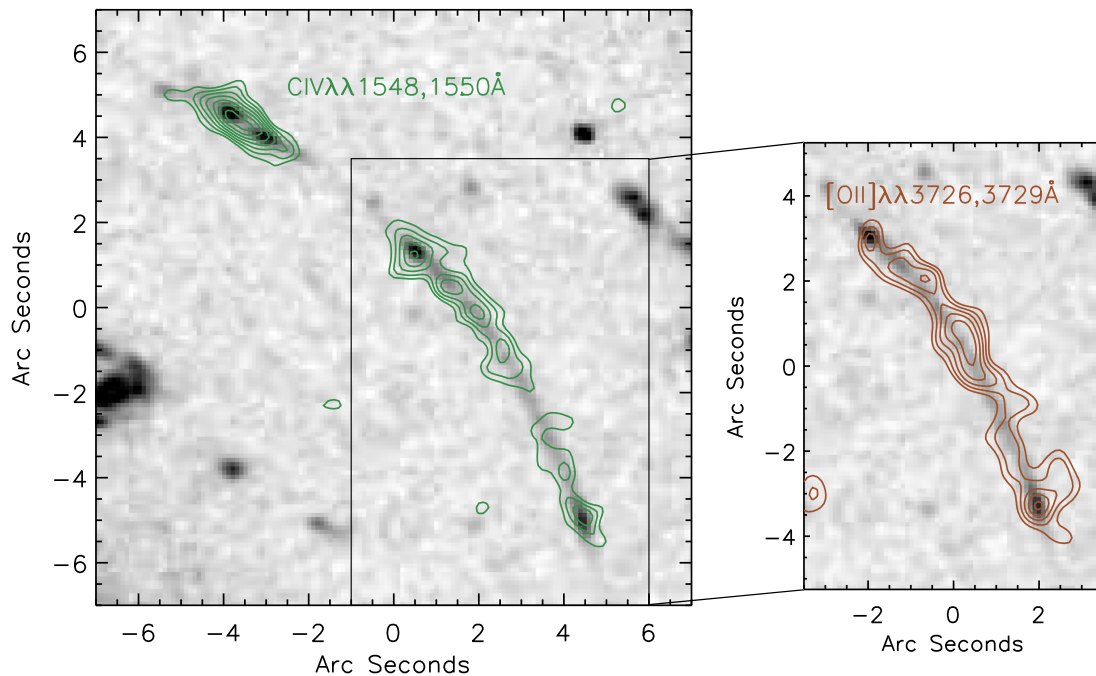


Figure 7. The spatial distribution of the C IV emission lines along the lensed galaxy images 1, 2 and 3 of the $z = 4.88$ arc (green contours, left-hand panel), compared to the [O II] distribution over the lensed images 2 and 3 from the SINFONI data (S07, brown contours, right-hand panel). The *HST* ($V_{666} + I_{814}$)-band image is shown in grey-scale. The high-ionization emission lines are spatially extended along the arc and trace the UV-continuum light. The morphologies of C IV and [O II] show similarities that might imply a nebular origin of C IV in a large number of the star-forming regions of the $z = 4.88$ arc.

high-ionization lines at $\sim -300 \text{ km s}^{-1}$, galactic feedback in this galaxy has possibly ejected a large fraction of the interstellar gas into the CGM/IGM.

The Si II $\lambda 1304 \text{ \AA}$ absorption appears to be weaker than the C IV $\lambda 1548 \text{ \AA}$ and Si IV $\lambda 1394 \text{ \AA}$ absorption lines. The ratio of the EW of the Si II $\lambda 1304 \text{ \AA}$ line over that of Si IV $\lambda 1394 \text{ \AA}$ is $\text{EW}(\text{Si II } \lambda 1304 \text{ \AA})/\text{EW}(\text{Si IV } \lambda 1394 \text{ \AA}) = 0.2$ (see Table 1). This is in contrast to the typical UV spectra of high-redshift galaxies, where the low-ionization lines are stronger than the high-ionization lines of the same species, with for example $\text{EW}(\text{Si II } \lambda 1304 \text{ \AA})/\text{EW}(\text{Si IV } \lambda 1394 \text{ \AA}) = 1.2$ in the composite spectrum of Lyman break galaxies by Shapley et al. (2003). We also fit the low- and high-ionization lines with a Gaussian profile convolved with a Voigt-profile absorber and estimate column densities of $\log N/\text{cm}^{-2} = 14.5 \pm 0.3$ and $\log N/\text{cm}^{-2} = 14.6 \pm 0.1$, respectively. Possibly a larger fraction of the outflowing gas is highly ionized due to a hard ionization field, which is present given the widespread nebular C IV $\lambda\lambda 1548, 1551 \text{ \AA}$ emission in the galaxy. It is possible that the neutral gas swept up by the ionized outflow is optically thin because of this, or else that the covering fraction of neutral gas in the CGM is incomplete (e.g. Erb 2015). To distinguish between these explanations, we would need a clean observation of the Si II $\lambda 1260 \text{ \AA}$ and Si II $\lambda 1527 \text{ \AA}$ absorption features, which are currently obscured by skylines.

3.2.5 Stellar population

Given that the C IV emission appears to be nebular in origin and powered by star formation (see Section 3.2.3), we investigate the properties of the stellar population that are needed to reproduce the $\sim 9 \text{ \AA}$ rest-frame EW nebular C IV emission.

Fig. 8 shows the evolution of the nebular C IV EW with metallicity, obtained from the Binary Population and Spectral Synthesis

(BPASS; Eldridge & Stanway 2012) models, using a single stellar population and including binary stellar evolution. The highly ionizing photons needed to generate the high-EW nebular C IV lines can be generated by a young stellar population (1–3 Myr old) with a low metallicity $Z = 0.05Z_{\odot}$.

The low-metallicity BPASS models also predict significantly reduced EW stellar P-Cygni profiles, due to the fact that the winds of hot stars are driven by metal-line absorption and therefore low-metallicity stars are much less efficient in driving stellar winds. This is consistent with the observed profile of C IV in the $z = 4.88$ arc (see Fig. 8), where we see no evidence for any redshifted stellar emission ($> 500 \text{ km s}^{-1}$) or broad blueshifted absorption ($< -500 \text{ km s}^{-1}$) from the systemic velocity. In fact, a lower EW stellar P-Cygni profile could provide an improved fit to our data, suggesting that the stellar iron abundance of the stellar population of the $z = 4.88$ arc could be even lower than that assumed in the lowest metallicity BPASS models available. The reasonable consistency between the stellar and nebular components in the C IV line profile provides confidence that we are indeed witnessing the early star formation in a galaxy with a very metal poor stellar population.

3.2.6 Kinematics

To derive spatially resolved dynamics of the stars and gas, we exploit the enhanced spatial resolution of the strongly lensed $z = 4.88$ arc and the IFU data to understand the spatial variation in the kinematics of the ISM/CGM.

In Fig. 9, we show the spatial variation of Ly α , C IV $\lambda\lambda 1548, 1551 \text{ \AA}$ and Si IV $\lambda\lambda 1394, 1403 \text{ \AA}$ along the lensed galaxy image 1 running from the north-east to south-west. We use galaxy image 1, since galaxy images 2 and 3 are incomplete images that cross the critical curve (see Fig. 1) and the stellar continuum of galaxy image 4 is not spatially resolved in the MUSE

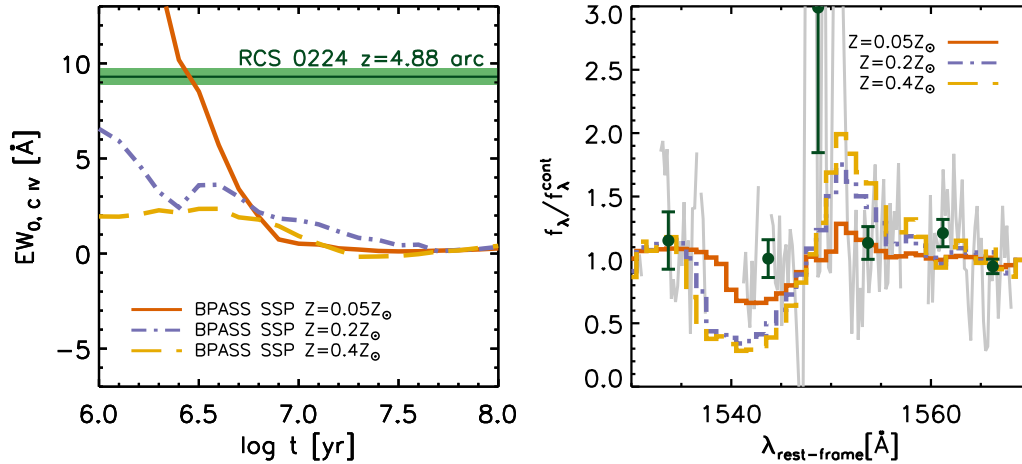


Figure 8. Left: predicted C IV EW evolution of nebular C IV emission during the first 100 Myr of a single stellar population at $Z = 0.05, 0.2, 0.4 Z_{\odot}$ metallicity (solid, dot-dashed and dashed lines, respectively) using the BPASS stellar population synthesis models including binary rotation (Eldridge & Stanway 2012). The green region indicates the rest-frame EW observed (including uncertainty) in the integrated spectrum of the $z = 4.88$ arc. The nebular C IV emission could be produced by a very low metallicity stellar population if the star clusters are observed during the first ~ 3 Myr of their lifetime. Right: a comparison of the stellar C IV profiles (excluding nebular emission) predicted by the same three BPASS models at 3 Myr with our data. The binned points on either side of the nebular C IV lines show no evidence for the strong P-Cygni profiles produced by stellar winds, indicating a metallicity of the stellar population lower than the $Z = 0.05 Z_{\odot}$ BPASS model.

data. The velocities in Fig. 9 are given with respect to a redshift of $z_{[O\text{II}]} = 4.8757$ obtained from galaxy images 2 and 3 (S07).

As noted in Section 3.2.2, the $\text{Ly}\alpha$ profile is not well described by a traditional Gaussian profile convolved with a Voigt-profile absorber and we therefore choose a non-parametric description of the $\text{Ly}\alpha$ profile. We characterize the spatial variation in the shape of the asymmetric $\text{Ly}\alpha$ profile by finding the wavelength that corresponds to 50 per cent, 25 per cent and 10 per cent of the peak flux redwards of the $\text{Ly}\alpha$ peak.

The C IV $\lambda\lambda 1548, 1551 \text{ \AA}$ emission lines are modelled using a Gaussian emission-line doublet. We model the Si IV $\lambda\lambda 1394, 1403 \text{ \AA}$ absorption-line doublet using Gaussians convolved with a Voigt-profile absorber. We detect these lines with $>5\sigma$ significance against the brightest continuum clump in galaxy image 1, corresponding to the north of the galaxy in the source plane. To obtain better constraints on the Si IV kinematics over the whole galaxy, we combine the bright clumps in galaxy images 1, 2 and 3 that correspond to the southern bright star-forming region in the source plane (we also show this in Fig. 1).

The C IV emission shows a velocity gradient of less than 50 km s^{-1} along the arc, with an irregular velocity pattern that is repeated in the lensed images 2 and 3. This is broadly consistent with the systemic velocity derived by S07, who find a velocity gradient in [O II] of $\lesssim 60 \text{ km s}^{-1}$. Moreover, the width of the C IV doublet does not change significantly as a function of position but stays either unresolved or marginally resolved at an FWHM $\sim 100 \text{ km s}^{-1}$.

For the high-ionization Si IV line, we derive a blueshift of $300\text{--}400 \text{ km s}^{-1}$ from the systemic redshift, consistent with the measured velocity offset by S07. The $\text{Ly}\alpha$ emission shows very little variation in the peak velocity, but broadens along the south-west side of the extended $\text{Ly}\alpha$ halo. This is consistent with the analysis in Section 3.2.1, which suggests a collimated high-velocity outflow on top of a halo of isotropically outflowing neutral gas. The small ($< 60 \text{ km s}^{-1}$) velocity gradient in the C IV and [O II] lines as well as the $\sim 100 \text{ km s}^{-1}$ velocity gradient in the Si IV absorption also support this picture of an outflow over the interpretation of large-scale rotation in the halo.

Comparing the high-ionization absorption features and the $\text{Ly}\alpha$ line, the $\text{Ly}\alpha$ peak produced by the receding outflow emits at significantly lower velocities ($< 100 \text{ km s}^{-1}$) than where the absorption of interstellar Si IV takes place in the approaching outflow ($300\text{--}400 \text{ km s}^{-1}$). This is in contradiction to a simple symmetric shell model (Verhamme et al. 2006; Gronke et al. 2015), which predicts that the $\text{Ly}\alpha$ peak be shifted by $\sim 2 \times \Delta v_{\text{exp}}$, where Δv_{exp} is the outflow velocity of the shell as measured from the interstellar absorption features. In this model, the $\text{Ly}\alpha$ peak velocity of the $z = 4.88$ arc would be expected at $\sim 600\text{--}800 \text{ km s}^{-1}$, a full order of magnitude higher than our observations (see Fig. 10). For comparison, the Shapley et al. (2003) composite spectrum of Lyman break galaxies at $z \sim 3$ shows a $\text{Ly}\alpha$ velocity offset of $+360 \text{ km s}^{-1}$ and low-ionization lines at -150 km s^{-1} , consistent with the symmetric shell model.

While some asymmetry could be present in the outflow, as indicated by the changing $\text{Ly}\alpha$ linewidth on one side of the galaxy, the peak velocity of $\text{Ly}\alpha$ changes by less than 50 km s^{-1} and it therefore seems unlikely that asymmetry in the outflowing gas explains the difference of hundreds of km s^{-1} between the approaching and receding gas tracers. We therefore suggest that a complex kinematic structure of the CGM, such as the velocity gradient we argued for in Section 3.2.2, must affect the absorption and escape of $\text{Ly}\alpha$ photons.

3.3 A physical picture for the $z = 4.88$ arc

In Section 3.2, we analysed the morphological and spectral properties of the $\text{Ly}\alpha$, C IV, Si IV and Si II emission and absorption lines in the $z = 4.88$ lensed galaxy arc behind RCS 0224–0002. Widespread nebular emission of the highly ionized C IV line implies that the source is an actively star-forming galaxy with a hard ionization field impacting upon the ISM surrounding the sites of star formation, while the blueshifted Si IV absorption line and spatially extended redshifted $\text{Ly}\alpha$ halo indicate galaxy-wide outflows.

A notable difficulty in this picture is the difference between the gas outflow velocities indicated by $\text{Ly}\alpha$ emission and by low-ionization absorption, suggesting that the two tracers are

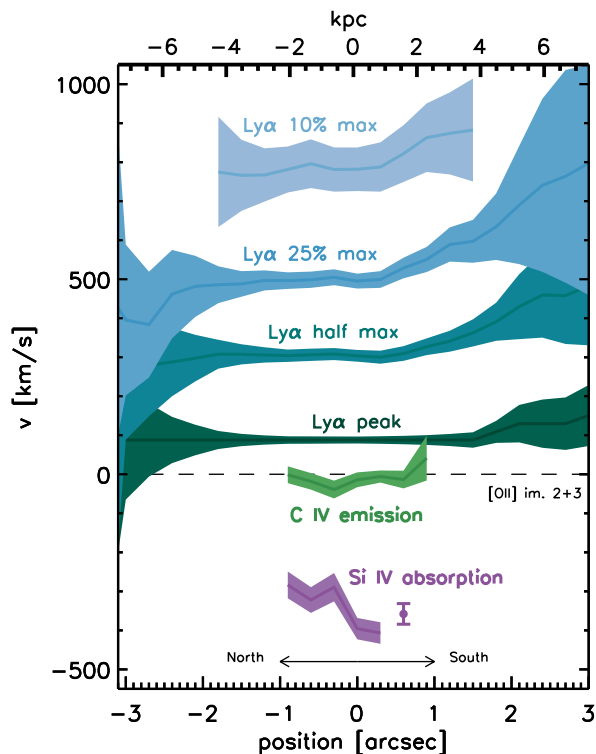


Figure 9. The spatial variation of the various line components along a tangential line through lensed image 1 of the $z = 4.88$ arc (from north-east to south-west in the image plane, corresponding to a line from north to south in the source plane) with respect to the [O II] redshift of $z = 4.8757$ measured from galaxy images 2 and 3. The C IV emission is close to the [O II] redshift, while the Si IV interstellar absorption lines are blueshifted by $\sim 300\text{--}400\text{ km s}^{-1}$ (the solid purple point corresponds to a measurement combining galaxy images 1, 2 and 3 to obtain a $>5\sigma$ line detection). The peak of the Ly α halo is redshifted by $\sim 80\text{ km s}^{-1}$, with very little velocity structure along the arc. The width of the Ly α line increases on one side of the galaxy as indicated by the positions of the half, 25 per cent and 10 per cent of the max flux in the line. We find no evidence of a strong velocity gradient in the nebular lines, and the peak of the Ly α emission stays nearly constant even beyond the galaxy. There is, however, a widening of the Ly α profile and a weak velocity gradient in the Si IV absorption, possibly indicating a collimated high-velocity outflow.

dominated by different parts of a CGM that hosts a complex kinematic gas structure (Section 3.2.6). To find a model that qualitatively describes the Ly α spectral properties, we argued for a strong velocity gradient in the gas (Section 3.2.2 and Appendix C), implying an accelerating outflow. In this model, the velocity gradient affects the column density seen by the Ly α photons at any given velocity, and the neutral gas at low velocity (and small radii) becomes transparent and produces the low-velocity Ly α peak, while a small fraction of the photons is scattered to the outer, high-velocity halo (see Fig. 11). This model could also explain the strong blueshift of the interstellar absorption lines compared to the peak of the Ly α emission, since these lines are absorbed by both low- and high-velocity gas. While we expect a similar high-velocity tail in the interstellar absorption lines as is present in the Ly α emission line, we do not have the S/N to confirm this prediction. Finally, the spatial extend of the Ly α halo, which is strongly centrally peaked but shows a faint extended wing, is also well described by this model.

Accelerating outflows have already been inferred in lower redshift studies (e.g. Martin & Bouché 2009; Weiner et al. 2009; Steidel et al. 2010). For example, Weiner et al. (2009) observed a

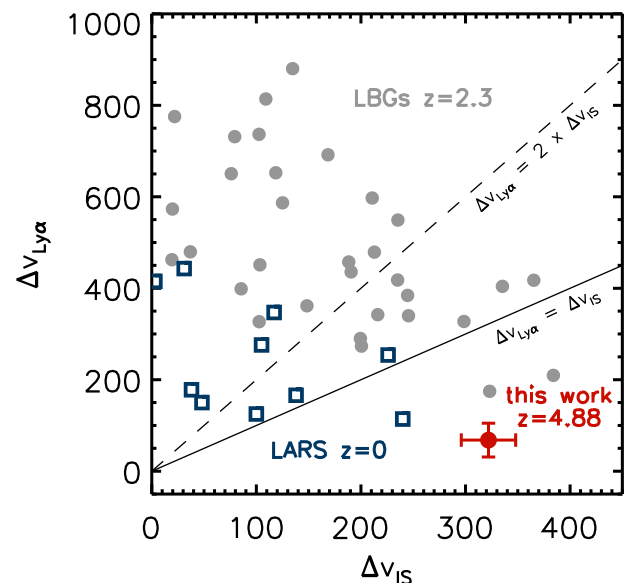


Figure 10. A comparison of the velocity offsets from the systemic redshift for the Ly α peak and the interstellar absorption line Si IV for the $z = 4.88$ arc and including similar measurements at $z = 0\text{--}2$ from the Ly α reference sample (LARS Rivera-Thorsen et al. 2015) and UV-selected star-forming galaxies observed with the LRIS spectrograph on Keck (Erb et al. 2006). A ‘shell’-like outflow is expected to have the Ly α peak be shifted by $\sim 2 \times \Delta v_{\text{IS}}$ (dashed line), while the $z = 4.88$ arc is among the very few galaxies with a Ly α peak shift below $\Delta v_{\text{Ly}\alpha} = \Delta v_{\text{IS}}$ (solid line).

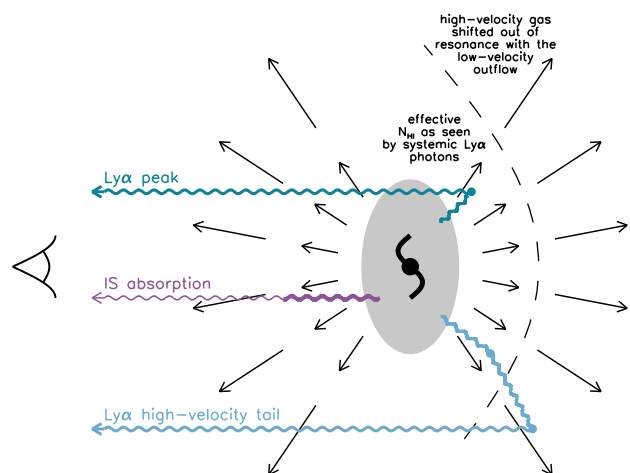


Figure 11. Schematic picture of the outflows, and Ly α and interstellar absorption features in the $z = 4.88$ arc. A strong velocity gradient in the outflow can produce the exponential Ly α line profile, due to the effective low column-density seen by photons emerging from the galaxy, while photons that get scattered into the higher velocity regions emerge as the lower luminosity high-velocity tail.

‘saw-tooth’ profile and a long, high-velocity tail in the Mg II absorption features of $0.4 < z < 1.4$ star-forming galaxies, which can be explained by accelerated cool gas. Martin & Bouché (2009) suggest that ultraluminous infrared galaxies at $z \sim 0.25$ have lower covering fractions for their higher velocity gas, implying that the highest velocity gas is found at the largest radii and therefore the presence of a velocity gradient in the outflow. Furthermore, Steidel et al. (2010) used UV-selected galaxy pairs at $z \sim 2\text{--}3$ to measure the typical gas covering fraction of outflowing gas as a function of

impact parameter and argued that consistency between the absorption line strength as a function of impact parameter, and the strength and profile shape of lines observed in the spectra of the galaxies, required large velocities and velocity gradients in the gas.

A physical explanation for accelerating gas is that the outflows are momentum driven (e.g. Murray, Quataert & Thompson 2005; Murray, Ménard & Thompson 2011). Momentum injection is thought to be provided by radiation pressure produced on the dust grains. However, recent studies using deep Atacama Large Millimetre Array (ALMA) observations (Coppin et al. 2015; Aravena et al. 2016; Bouwens et al. 2016; Dunlop et al. 2016) have shown that low-mass high-redshift galaxies have low dust content and the $z = 4.88$ arc does not appear heavily reddened (i.e. the continuum is bluer than that observed in the composite spectrum of Shapley et al. 2003, see Fig. 2), indicating that only a small fraction of the star formation radiation is available to drive winds. Murray et al. (2005) also consider momentum injection through ram pressure by supernovae, which can deposit roughly the same amount of momentum as the radiation pressure on the dust and is therefore potentially a more likely source of momentum injection. Alternatively, Haehnelt (1995) considers momentum transfer due to the radiation of ionizing photons, which could be a preferred source of momentum injection given the hard ionization radiation field we know is present throughout the galaxy, because of the wide-spread high-EW C IV emission.

In summary, a physical picture consistent with our observations is that of a vigorously star-forming galaxy, inducing a galaxy-wide momentum-driven wind, either due to supernova ram pressure or to the strong radiation field.

3.3.1 Comparison with UV properties of sources at $z \lesssim 3$

To date, only a small sample of high-redshift galaxies have been studied with high S/N rest-frame UV spectroscopy and all below $z < 4$, due to their faintness and hence the long integration times needed to detect faint spectral features. Therefore, we will compare the $z = 4.88$ arc with lower redshift sources in order to understand if the features observed in this arc are common in $z \lesssim 3$ galaxies, or if there is evidence for a change in the ISM/CGM properties of galaxies as we start observing sources at higher redshifts.

The brightest targets for rest-frame UV studies at $z \sim 2-3$ are identified from ground-based surveys, which select strongly lensed galaxies, that are often relatively massive ($M_* > 10^{9.5} M_\odot$) and strongly star-forming (SFR $\gtrsim 50 M_\odot \text{ yr}^{-1}$), including cB58 ($z = 2.73$; Pettini et al. 2000, 2002), the Cosmic Eye ($z = 3.07$; Smail et al. 2007; Quider et al. 2010), the Cosmic Horseshoe ($z = 2.38$; Quider et al. 2009) and SGAS J105039.6+001730 ($z = 3.63$; Bayliss et al. 2014). Typical UV-spectroscopic signatures in these massive galaxies include strong P-Cygni profiles seen in the C IV line profile, strong low-ionization absorption features with respect to high-ionization ISM lines of the same species and a wide velocity range for both low- and high-ionization absorption lines (FWHM $\sim 500-1000 \text{ km s}^{-1}$). This is in strong contrast to the $z = 4.88$ arc, where we detect no evidence for stellar winds through the C IV P-Cygni line and also where the high-ionization ISM absorption lines are only a few hundred km s^{-1} wide, indicating a marked difference in the properties of the stellar winds and the galaxy outflows of our source.

A few of these massive galaxies show strong C III] $\lambda\lambda 1907, 1909 \text{ \AA}$ emission, an uncommon feature in local galaxies (e.g. Rigby et al. 2015) as it requires a significant flux above 24 eV and therefore

indicates that these high-redshift galaxies have harder ionization fields and/or higher ionization parameters compared to their local counterparts. However, the nebular C IV $\lambda\lambda 1548, 1551 \text{ \AA}$ doublet in the $z = 4.88$ arc (which is only seen when significant amount of flux above 48 eV is produced) is typically not detected.

With a dynamical mass of $\sim 10^{10} M_\odot$ and SFR of $12 M_\odot \text{ yr}^{-1}$ (see S07), the $z = 4.88$ arc behind RCS 0224–0002 might be more likely to share similar properties to lower mass sources such as the Lynx arc ($z = 3.36$; Holden et al. 2001; Fosbury et al. 2003), BX418 ($z = 2.3$; Erb et al. 2010) and a sample of $z = 1.4-2.9$ galaxies behind Abell 1689 and MACS 0451 targeted by Stark et al. (2014). Indeed, the Lynx arc and 3 of the 17 galaxies in the Stark et al. (2014) all show evidence for narrow C IV. Erb et al. (2010) also require a significant contribution from nebular C IV emission as well as stellar P-Cygni emission to explain their observations.

Due to the faintness of most of these low-mass sources, a detailed analysis of the absorption features is rarely possible. Stark et al. (2014), however, notice an almost complete absence of P-Cygni and ISM absorption features in the galaxies where they do detect the continuum (similar to local galaxies selected on their low oxygen abundance presented by Berg et al. 2016). Furthermore, Erb et al. (2010) are able to detect numerous absorption features in BX418 at $z = 2.3$, due to an extremely deep integration, and find that the low-ionization absorption lines in this galaxy are typically significantly weaker than the high-ionization ISM lines, similar to the $z = 4.88$ arc. An obvious difference between BX814 and the $z = 4.88$ arc behind RCS 0224–0002 is the spectral shape of Ly α ; BX814 has an extremely broad, FWHM $\sim 850 \text{ km s}^{-1}$, Ly α line, as opposed to FWHM $< 300 \text{ km s}^{-1}$ observed in this galaxy. Furthermore, in BX814, the peak Ly α emerges at $\Delta v \sim +300 \text{ km s}^{-1}$, more than three times higher than for the $z = 4.88$ arc, while the interstellar absorption lines show a 1.5–2 times lower velocity offset ($\Delta v \sim -150 \text{ km s}^{-1}$).

In summary, there appear significant differences in the nebular lines, stellar and ISM absorption features between the $z = 4.88$ arc behind RCS 0224–0002 and lower redshift sources with masses above $M_* > 10^{9.5} M_\odot$. Typically, low-mass sources and/or low-metallicity galaxies at $z < 3$ can in some cases have very similar highly ionized nebular features and some similar features in the absorption lines of low-mass galaxies have been detected as well; however, no galaxy spectrum or composite spectrum of galaxies matches the full set of observations of the $z = 4.88$ arc, highlighting the need for larger samples of high S/N observations of very high redshift galaxies in order to understand if the physical properties of the earliest systems are systematically different from their later time counterparts or if the $z = 4.88$ arc is a rare outlier in the $z \sim 5$ galaxy population.

3.3.2 Implications for reionization studies

Whether galaxies can reionize the Universe and what sources contribute most to reionization, depends on a large number of parameters, including the Lyman-continuum photon production efficiency of galaxies, ξ_{ion} , and the escape fraction of ionizing photons (Bouwens et al. 2015b; Robertson et al. 2015). While determining the physical properties of galaxies in the reionization epoch remains challenging, recent spectroscopy of $z \gtrsim 7$ galaxies has shown evidence for strong rest-frame UV nebular emission lines such as C IV $\lambda\lambda 1548, 1551 \text{ \AA}$ (Stark et al. 2015, 2017). *Spitzer*/IRAC imaging studies have also inferred extremely strong [O III] $\lambda\lambda 4959, 5007 \text{ \AA}$ in the rest-frame optical spectra of typical $z \sim 7-8$ galaxies (Labbé

et al. 2013; Smit et al. 2014, 2015; Roberts-Borsani et al. 2016). These results suggest that galaxies in the reionization epoch could have similar hard radiation field and/or high-ionization parameter as the $z = 4.88$ arc and it is therefore interesting to assess this galaxy as an analogue of the sources that might be responsible for reionization.

Using the BPASS stellar population template of a young extremely low metallicity galaxy needed to match the C IV EW (see Section 3.2.5), we derive a Lyman-continuum photon production efficiency in the $z = 4.88$ arc of $\log_{10} \xi_{\text{ion}} = 25.74 \text{ Hz erg}^{-1}$, 0.63 dex higher than the canonical value of $\log_{10} \xi_{\text{ion}} = 25.11 \text{ Hz erg}^{-1}$ (Kennicutt 1998). Systemic deviations of ~ 0.1 dex from the canonical value of ξ_{ion} have been derived from the inferred H α emission in typical $z \sim 4\text{--}5$ UV-selected galaxies (Bouwens et al. 2016; Rasappu et al. 2016; Smit et al. 2016). The bluest $z \sim 4\text{--}5$ galaxies ($\beta < -2.3$), likely very young and dust-free sources, have a significantly higher Lyman-continuum photon production efficiency of $\log_{10} \xi_{\text{ion}} = 25.53\text{--}25.78 \text{ Hz erg}^{-1}$ (Stark et al. 2015; Bouwens et al. 2016), in good agreement with our derived value for the $z = 4.88$ arc, which also has a blue UV-continuum colour ($\beta = -2.2$). If similarly young and low-metallicity galaxies are common at $z \gtrsim 7$, they could contribute significantly to reionization even for modest ($\lesssim 5$ per cent) escape fractions.

Measuring the direct escape of Lyman-continuum photons at $z \sim 5$ is challenging due to the intervening Ly α forest in the IGM. However, the Si II $\lambda 1304 \text{ \AA}$ absorption in the $z = 4.88$ arc shows no sign of absorption at the systemic velocity by low-ionization gas in the ISM, indicating Lyman-continuum photons might also easily escape. Furthermore, the collimated high-velocity outflow discussed in Section 3.2.2 could blow holes into the ISM through which the photons preferentially escape (see Erb 2015).

Another important implication of the $z = 4.88$ arc as a $z \gtrsim 7$ galaxy analogue, is the opportunity to identify similar sources with future facilities such as the *James Webb Space Telescope* and the various Extremely Large Telescopes. Most of the Ly α emission of galaxies in the reionization epoch will be absorbed due to the surrounding neutral IGM, but strong nebular lines such as C IV $\lambda\lambda 1548, 1551 \text{ \AA}$ (seen at an observed EW of $\sim 80 \text{ \AA}$ at $z \sim 8$) can be easily identified. While these lines are uncommon in the local Universe, our results indicate that these lines are widely produced by the young and low-metallicity stellar population within the $z = 4.88$ arc. These characteristics are likely to be more common as we start observing galaxies at earlier epochs.

4 A BLIND SEARCH FOR HIGH-REDSHIFT Ly α EMITTERS

Finally, we can use the relatively wide field of view of MUSE to search for other emitters in the field. Deep MUSE observations in the *Hubble deep fields* have proven efficient in detecting Ly α out to redshift $z \sim 6.6$ (e.g. Bacon et al. 2015). The extremely faint or undetected *HST* counterparts of these high-redshift Ly α emitters indicate that we are sensitive to the faint end of the UV luminosity function, sources with similar properties to the galaxies expected to be responsible for cosmic reionization. While these observations require integration times of ~ 30 h, similar sources can potentially be found behind by strong lensing clusters within reasonable integrations times (e.g. Karman et al. 2015; Bina et al. 2016).

Due to its high mass, relative compactness and high-redshift RCS 0224–0002 appears to be an efficient lens for high-redshift galaxies. Unlike low-redshift strong-lensing clusters, our single MUSE pointing covers the entire $z \sim 6$ critical curves

of RCS 0224–0002. We therefore explore the potential of RCS 0224–0002 as a window into the very high redshift Universe. We search for emission-line candidates in our MUSE data set in three windows with low sky contamination, 7100–7200 \AA , 8070–8270 \AA and 9060–9300 \AA , corresponding to Ly α redshift ranges of $z = 4.84\text{--}4.92$, $z = 5.64\text{--}5.80$ and $z = 6.54\text{--}6.65$, respectively. To achieve this, we develop a blind line-detection method that follows a number of consecutive steps to identify extremely faint sources, while minimizing spurious detections. First, for each pixel in the MUSE field of view (masking bright continuum sources and removing cluster galaxies from the sample), we extract a one-dimensional spectrum by averaging 5×5 pixels, where we use the PSF measured from the MUSE data to assign a weight to each of the pixels. For each of the one-dimensional spectra, we search for individual spectral pixels that have a value $> 3.5\sigma$ above the noise (estimated from the same one-dimensional spectrum, but masking the skylines) to identify potential lines. For each candidate, we fit a single Gaussian profile to the spectrum and we require a $\Delta\chi^2 \geq 7.5^2$ between the Gaussian and a straight line fit with a constant value.

To remove spurious detections, we next generate a $12 \text{ arcsec} \times 12 \text{ arcsec}$ continuum-subtracted narrow-band image around the line. We create this image by extracting the images from the cube with a wavelength within the FWHM of the line (as measured from the Gaussian profile fit) and averaging them, we then subtract the median continuum in two bands (20 \AA wide) at each side of the line (20 \AA removed from the centre). On the continuum-subtracted narrow-band image, we measure 1000 randomly selected point-source fluxes, using the PSF extracted from an isolated star in the MUSE continuum image to weight the pixels around each point. We require the line candidates to have a flux $\geq 3\sigma$ above the randomly sampled point-source flux distribution.

We visually inspect our line candidates and remove all sources that are clearly [O II], [O III] or H α emission, and we remove low-redshift interlopers when bright continuum flux is detected blueward of the rest-frame 912 \AA limit (based on the Ly α redshift). Note that while we do not exclude sources that show continuum flux between rest-frame 912 \AA and 1216 \AA , we detect flux below the rest-frame 1216 \AA break in only one Ly α candidate (RCS0224_LAEz4p8773) from our final sample. Furthermore, we remove sources that appear due to noise artefacts at the edges of the CCDs, or sources that are strongly affected by an uneven background.

A significant uncertainty in our interloper rejection is that almost none of our Ly α candidates are detected in the *HST/ACS+WFC3* imaging, and therefore no prior based on photometric redshift of the sources can be applied to our Ly α selection. Furthermore, many of our Ly α candidates are observed with too low S/N to identify the expected asymmetric Ly α spectral line shape and therefore our sample could be contaminated by for example high-EW [O III] $\lambda 5007 \text{ \AA}$ lines of lower redshift galaxies, for which the [O III] $\lambda 4959 \text{ \AA}$ line is too faint to be detected.

To make an estimate of the number of spurious detections we expect in our blind search, we perform a test for false-positives by running our source-selection code on the inverted data cube. To identify a ‘pure’ sample, we calculate the S/N required in the algorithm to give a false positive rate of zero; which is $\Delta\chi^2 \geq 7.5^2$ for the line fit and $\geq 3\sigma$ for the continuum-subtracted point-source flux.

In our final sample of Ly α candidates, we have five sources at $z \sim 4.8$, eight sources at $z \sim 5.7$ and one source at $z \sim 6.6$. The sources are listed in Table D1 and thumbnails of all the sources presented in Appendix D. For comparison, in a 30 h exposure over

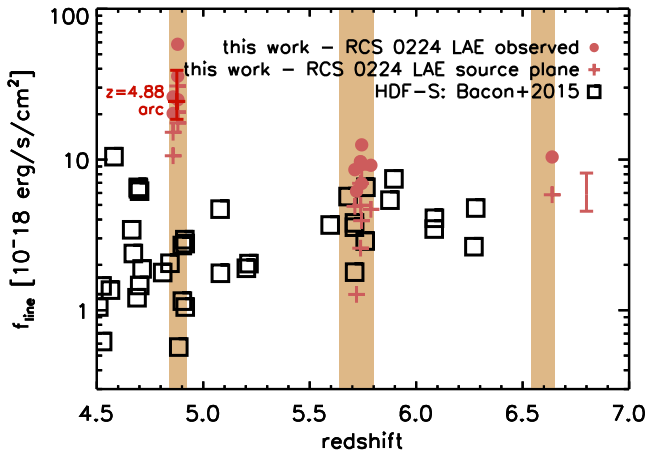


Figure 12. A comparison of observed and intrinsic flux of Ly α emitters in the HDF-S from Bacon et al. (2015) with our blind search in the RCS 0224–0002 MUSE field. The typical uncertainty on the intrinsic fluxes is indicated by the errorbars on the right. The shaded regions indicate our search windows, which have low sky contamination. Comparing our 3.75 h integration to the 27 h MUSE integration by Bacon et al. (2015), we are able to detect similarly faint sources in the source plane, that is amplified by the cluster lensing.

a 1 arcmin² field over the HDF-S Bacon et al. (2015) find for the same redshift intervals seven Ly α emitters at $z \sim 4.8$, six emitters at $z \sim 5.7$ and no emitters at $z \sim 6.6$, see Fig. 12. Using a 4 h exposure and 1 arcmin² field, Karman et al. (2015) find only one (multiply lensed) source above $z > 4.5$ behind the Frontier Fields cluster Abell S1063.

A notable result from our blind search for Ly α line candidates is the presence of a large number of bright Ly α emitting sources at $z \sim 4.88$. Three bright sources at $2.5\text{--}5.8 \times 10^{-17}$ erg s⁻¹ cm⁻² are located at $\sim +250\text{--}300$ km s⁻¹ or ~ 200 kpc from the bright arc, while two more sources are located ~ -1000 km s⁻¹ or ~ 1.7 Mpc from the arc. With the exception of one of these sources, none of the line emitters are detected in the *HST* imaging (at $>5\sigma$); however, they all exhibit a clear asymmetric line profile that provides evidence of these sources being Ly α emitters. After correcting for the lensing magnification, these sources have Ly α line luminosities $\sim 1\text{--}3 \times 10^{-17}$ erg s⁻¹ cm⁻² ($L = 2.6\text{--}5.1 \times 10^{42}$ erg s⁻¹), $\sim 2\text{--}10 \times$ brighter than sources found in the HDF-S by Bacon et al. (2015) at the same redshift. Comparing to the faint end of the Ly α luminosity functions obtained through narrow-band surveys at $z = 3.5\text{--}5.7$ (e.g. Ouchi et al. 2008; Santos, Sobral & Matthee 2016), we would predict 0.1–0.9 Ly α emitters as bright as $\log L/\text{erg s}^{-1} = 42.5$ in our MUSE data in the redshift window $z = 4.84\text{--}4.92$. This suggests that either the Ly α luminosity function is steeper at the faint-end than measured in narrow-band surveys (see also Drake et al. 2016), or else that the $z = 4.88$ arc is located in an $\sim 7\text{--}60 \times$ overdense region, or group.

5 SUMMARY

We present a survey for line-emitter galaxies behind the strong lensing cluster RCS 0224–0002. We analyse the rest-frame UV spectrum of a lensed galaxy magnified 29 times at $z = 4.88$. For this source, we observe the following properties:

(i) The $z = 4.88$ galaxy is surrounded by a spatially extended Ly α halo with an exponential spatial profile. The spectral properties of the Ly α halo are spatially uniform, showing a single redshifted peak

close to the systemic velocity ($\Delta v < 100$ km s⁻¹) and high-velocity tail ($\Delta v > 1000$ km s⁻¹). The spatial and spectral properties of the halo are consistent with resonantly scattered Ly α photons produced in a central source and backscattered in a receding outflow from the galaxy.

(ii) We detect spatially resolved narrow C IV $\lambda\lambda 1548, 1551$ Å emission. The spatial distribution of C IV strongly resembles that of the [O II] line, suggesting a nebular origin of the line, powered by star formation. We argue that the strong C IV emission ($EW_0 \sim 9$ Å) can be reproduced with a young ($t < 5$ Myr), low-metallicity ($Z \lesssim 0.05Z_{\odot}$) stellar population. The blue UV-continuum colour ($\beta = -2.2$) and the absence of a P-Cygni profile, indicating low-metallicity stars with significantly reduced stellar winds, is consistent with this analysis.

(iii) We observe strong high-ionization interstellar absorption lines in C IV and S IV with a significant blueshift ($\Delta v \sim 300$ km s⁻¹) from the systemic velocity and much weaker low-ionization S II absorption ($EW(\text{Si II } \lambda 1304 \text{ Å})/EW(\text{Si IV } \lambda 1394 \text{ Å}) = 0.2$). The blueshift of the interstellar lines is surprising when considering how close to the systemic velocity we observe the Ly α line and given that an outflowing shell model suggests $\Delta v_{\text{IS}} \sim v_{\text{shell}}$ and $\Delta v_{\text{Ly}\alpha} \sim 2 \times v_{\text{shell}}$.

We propose a physical model for this galaxy in which the outflowing gas follows a strong velocity gradient such that the effective column density of neutral gas, as seen by the outwards scattering Ly α photons, is significantly reduced, allowing for Ly α to escape at much lower velocities than the mean gas outflow (see Verhamme et al. 2006). This velocity gradient likely requires a momentum ejection into the gas, which can originate from supernovae ram pressure or radiation pressure (e.g. Murray et al. 2005). These results emphasize the importance of increasing the samples of high-redshift low-mass galaxies where we are able to detect the interstellar absorption features, as relying on Ly α as a tracer of galaxy outflows can significantly underestimate the feedback in galaxies such as the $z = 4.88$ arc behind RCS 0224.

We perform a blind line search for high-redshift Ly α using three wavelength ranges that are relatively free of sky lines, corresponding to $z_{\text{Ly}\alpha} = 4.84\text{--}4.92$, $z_{\text{Ly}\alpha} = 5.64\text{--}5.80$ and $z_{\text{Ly}\alpha} = 6.54\text{--}6.65$. We select sources above the significance level needed such that a line search on the inverted data results in zero false positives. We find a total of 14 Ly α candidates, of which only one is detected in the *HST* imaging. This suggests that line surveys over strong lensing clusters with MUSE are efficient at finding ultrafaint galaxies out to $z \sim 6.6$ and hence study the properties of faint Ly α emitting galaxies that are likely to have contributed to reionization.

ACKNOWLEDGEMENTS

We are grateful to Graham Smith for recovering the parameters of the S07 lensing model. We thank Matthew Hayes, Bethan James, Vera Patricio, Max Pettini, Tom Theuns, Ryan Trainor and Anne Verhamme for useful discussions. We are grateful to Max Gronke for giving us access to the on-line tool TLAC_WEB. RS, AMS, RJM and IRS acknowledge support from STFC (ST/L0075X/1). RS and IRS also acknowledge support from the ERC Advanced Investigator programme DUSTYGAL 321334. In addition, RS acknowledges support from the Leverhulme Trust, AMS from an STFC Advanced Fellowship (ST/H005234/1), RJM acknowledges support from a Royal Society URF and IRS acknowledges support from a Royal Society/Wolfson Merit Award. JPK acknowledges support from the ERC advanced grant LIDA and from CNRS. This work was

partially based on observations made with the NASA/ESA *Hubble Space Telescope*, obtained at the Space Telescope Science Institute, which is operated by the Association of Universities for Research in Astronomy, Inc., under NASA contract NAS 5-26555. These observations are associated with program #14497.

REFERENCES

- Amorín R. et al., 2017, preprint ([arXiv:1701.04416](https://arxiv.org/abs/1701.04416))
- Aravena M. et al., 2016, *ApJ*, 833, 68
- Bacon R. et al., 2010, *SPIE*, 7735, 773508
- Bacon R. et al., 2015, *A&A*, 575, A75
- Bayliss M. B. et al., 2014, *ApJ*, 790, 144
- Berg D. A., Skillman E. D., Henry R. B. C., Erb D. K., Carigi L., 2016, *ApJ*, 827, 126
- Bina D. et al., 2016, *A&A*, 590, A14
- Bouwens R. J. et al., 2015a, *ApJ*, 803, 34
- Bouwens R. J. et al., 2015b, *ApJ*, 811, 140
- Bouwens R. J. et al., 2016, *ApJ*, 833, 72
- Bouwens R. J. et al., 2016, *ApJ*, 831, 176
- Bowler R. A. A. et al., 2015, *MNRAS*, 452, 1817
- Caminha G. B. et al., 2016, *A&A*, 595, A100
- Christensen L. et al., 2012b, *MNRAS*, 427, 1973
- Coppin K. E. K. et al., 2015, *MNRAS*, 446, 1293
- Dijkstra M., Loeb A., 2009, *MNRAS*, 400, 1109
- Dijkstra M., Haiman Z., Spaans M., 2006, *ApJ*, 649, 14
- Drake A. B. et al., 2016, *MNRAS*, preprint ([arXiv:1609.02920](https://arxiv.org/abs/1609.02920))
- Dunlop J. S. et al., 2016, *MNRAS*, 466, 861
- Eldridge J. J., Stanway E. R., 2012, *MNRAS*, 419, 479
- Erb D. K., 2015, *Nature*, 523, 169
- Erb D. K. et al., 2006, *ApJ*, 646, 107
- Erb D. K. et al., 2010, *ApJ*, 719, 1168
- Faucher-Giguère C.-A., Kereš D., Dijkstra M., Hernquist L., Zaldarriaga M., 2010, *ApJ*, 725, 633
- Feltre A., Charlot S., Gutkin J., 2016, *MNRAS*, 456, 3354
- Finkelstein S. L. et al., 2015, *ApJ*, 810, 71
- Fosbury R. A. E. et al., 2003, *ApJ*, 596, 797
- Giallongo E. et al., 2015, *A&A*, 578, A83
- Giavalisco M. et al., 2004, *ApJ*, 600, L103
- Gladders M. D., Yee H. K. C., Ellingson E., 2002, *AJ*, 123, 1
- Gronke M., Bull P., Dijkstra M., 2015, *ApJ*, 812, 123
- Gullberg B. et al., 2016, *A&A*, 586, A124
- Haehnelt M. G., 1995, *MNRAS*, 273, 249
- Hainline K. N., Shapley A. E., Greene J. E., Steidel C. C., 2011, *ApJ*, 733, 31
- Hayes M. et al., 2013, *ApJ*, 765, L27
- Holden B. P. et al., 2001, *AJ*, 122, 629
- Jones T., Stark D. P., Ellis R. S., 2012, *ApJ*, 751, 51
- Jullo E., Kneib J.-P., 2009, *MNRAS*, 395, 1319
- Jullo E., Kneib J.-P., Limousin M., Elíasdóttir Á., Marshall P. J., Verdugo T., 2007, *New J. Phys.*, 9, 447
- Karman W. et al., 2015, *A&A*, 574, A11
- Kennicutt R. C., Jr1998, *ARA&A*, 36, 189
- Kneib J.-P., Ellis R. S., Smail I., Couch W. J., Sharples R. M., 1996, *ApJ*, 471, 643
- Labbé I. et al., 2013, *ApJ*, 777, L19
- Lehnert M. D., Bremer M., 2003, *ApJ*, 593, 630
- Leitherer C., Leão J. R. S., Heckman T. M., Lennon D. J., Pettini M., Robert C., 2001, *ApJ*, 550, 724
- Madau P., Ferguson H. C., Dickinson M. E., Giavalisco M., Steidel C. C., Fruchter A., 1996, *MNRAS*, 283, 1388
- Martin C. L., Bouché N., 2009, *ApJ*, 703, 1394
- Matsuda Y. et al., 2012, *MNRAS*, 425, 878
- McLure R. J., Cirasuolo M., Dunlop J. S., Foucaud S., Almaini O., 2009, *MNRAS*, 395, 2196
- Meneghetti M. et al., 2016, preprint ([arXiv:1606.04548](https://arxiv.org/abs/1606.04548))
- Momose R. et al., 2014, *MNRAS*, 442, 110
- Murray N., Quataert E., Thompson T. A., 2005, *ApJ*, 618, 569
- Murray N., Ménard B., Thompson T. A., 2011, *ApJ*, 735, 66
- Oke J. B., Gunn J. E., 1983, *ApJ*, 266, 713
- Ouchi M. et al., 2004, *ApJ*, 611, 660
- Ouchi M. et al., 2008, *ApJS*, 176, 301
- Patrício V. et al., 2016, *MNRAS*, 456, 4191
- Petrosian V., 1976, *ApJ*, 209, L1
- Pettini M., Steidel C. C., Adelberger K. L., Dickinson M., Giavalisco M., 2000, *ApJ*, 528, 96
- Pettini M., Rix S. A., Steidel C. C., Adelberger K. L., Hunt M. P., Shapley A. E., 2002, *ApJ*, 569, 742
- Quider A. M., Pettini M., Shapley A. E., Steidel C. C., 2009, *MNRAS*, 398, 1263
- Quider A. M., Shapley A. E., Pettini M., Steidel C. C., Stark D. P., 2010, *MNRAS*, 402, 1467
- Rasappu N., Smit R., Labbé I., Bouwens R. J., Stark D. P., Ellis R. S., Oesch P. A., 2016, *MNRAS*, 461, 3886
- Rigby J. R., Bayliss M. B., Gladders M. D., Sharon K., Wuyts E., Dahle H., Johnson T., Peña-Guerrero M., 2015, *ApJ*, 814, L6
- Rivera-Thorsen T. E. et al., 2015, *ApJ*, 805, 14
- Roberts-Borsani G. W. et al., 2016, *ApJ*, 823, 143
- Robertson B. E., Ellis R. S., Furlanetto S. R., Dunlop J. S., 2015, *ApJ*, 802, L19
- Rosdahl J., Blaizot J., 2012, *MNRAS*, 423, 344
- Santos S., Sobral D., Matthee J., 2016, *MNRAS*, 463, 1678
- Sawicki M. J., Lin H., Yee H. K. C., 1997, *AJ*, 113, 1
- Shapley A. E., Steidel C. C., Pettini M., Adelberger K. L., 2003, *ApJ*, 588, 65
- Smail I. et al., 2007, *ApJ*, 654, L33
- Smit R. et al., 2014, *ApJ*, 784, 58
- Smit R. et al., 2015, *ApJ*, 801, 122
- Smit R. et al., 2016, *ApJ*, 833, 254
- Stark D. P. et al., 2014, *MNRAS*, 445, 3200
- Stark D. P. et al., 2015, *MNRAS*, 454, 1393
- Stark D. P. et al., 2017, *MNRAS*, 464, 469
- Steidel C. C., Giavalisco M., Pettini M., Dickinson M., Adelberger K. L., 1996, *ApJ*, 462, L17
- Steidel C. C., Adelberger K. L., Giavalisco M., Dickinson M., Pettini M., 1999, *ApJ*, 519, 1
- Steidel C. C., Erb D. K., Shapley A. E., Pettini M., Reddy N., Bogosavljević M., Rudie G. C., Rakic O., 2010, *ApJ*, 717, 289
- Steidel C. C., Bogosavljević M., Shapley A. E., Kollmeier J. A., Reddy N. A., Erb D. K., Pettini M., 2011, *ApJ*, 736, 160
- Swinbank A. M., Bower R. G., Smith G. P., Wilman R. J., Smail I., Ellis R. S., Morris S. L., Kneib J.-P., 2007, *MNRAS*, 376, 479 (S07)
- Swinbank A. M. et al., 2015, *MNRAS*, 449, 1298
- van der Burg R. F. J., Hildebrandt H., Erben T., 2010, *A&A*, 523, A74
- Vanzella E. et al., 2016, *ApJ*, 821, L27
- Vanzella E. et al., 2017, *MNRAS*, 465, 3803
- Verhamme A., Schaerer D., Maselli A., 2006, *A&A*, 460, 397
- Weiner B. J. et al., 2009, *ApJ*, 692, 187
- Wisotzki L. et al., 2016, *A&A*, 587, A98

APPENDIX A: BEST-FITTING PARAMETERS OF THE LENS MODEL

In Section 3.1, we described the set-up and main results of our `LENSTOOL` modelling. In this appendix, we present the full observational constraints in Table A1 and the best-fitting parameters of the lensing model that is used in this work in Table A2.

Table A1. Input locations of strong lens multiple images [RA, Dec.], uncertainty on the position (arcsec), redshift. The redshift of system D is left free, and constrained during the fit to be >5.3 (1σ).

ID	RA	Dec.	Δ (arcsec)	z
A1	36.140826	-0.038235783	0.2	4.88
A2	36.139833	-0.039005229	0.2	4.88
A3	36.138742	-0.040753058	0.2	4.88
A4	36.14349	-0.042785468	0.2	4.88
B1	36.144748	-0.042371596	0.2	2.395
B2	36.145091	-0.041225429	0.2	2.395
B3	36.143675	-0.039536976	0.8	2.395
B4	36.141663	-0.039894484	0.8	2.395
B5	36.140316	-0.043556393	0.8	2.395
B6	36.142475	-0.041860145	0.2	2.395
C1	36.14525	-0.03783889	0.8	5.498
C2	36.141739	-0.043416674	0.2	5.498
D1	36.13902	-0.043164193	0.8	-
D2	36.142798	-0.03823784	0.8	-
D3	36.140498	-0.03920681	0.8	-

Table A2. Parameters of best-fitting mass model. Angles of the major axis are anticlockwise from north.

Δ RA (arcsec)	Δ Dec. (arcsec)	v_{disp} (km s^{-1})	ϵ	θ (deg)	r_{core} (kpc)	r_{cut} (kpc)
-1.80	3.80	624.7	0.57	128	40.01	1000.0
0.00	0.00	385.7	0.57	11	14.61	1000.0
-1.29	2.23	190.3	0.16	29	0.51	77.4
4.16	5.43	186.9	0.59	41	0.51	74.6
0.90	0.83	179.7	0.11	16	0.51	69.0
-18.34	0.73	169.2	0.37	134	0.41	61.2
18.07	-6.62	148.4	0.04	158	0.31	47.1
-5.43	-11.29	141.4	0.21	33	0.31	42.8
-18.91	-11.12	138.5	0.41	122	0.31	41.0
-9.24	21.64	137.6	0.13	45	0.31	40.5
7.70	4.51	136.3	0.02	151	0.31	39.7
8.97	4.08	133.2	0.29	44	0.31	37.9
-25.95	2.73	130.2	0.02	133	0.21	36.2
0.53	22.22	122.6	0.26	60	0.21	32.1
17.33	-2.41	119.8	0.18	60	0.21	30.7
-22.75	7.69	119.5	0.17	52	0.21	30.5
-15.24	-5.12	111.0	0.30	45	0.21	26.4
-0.42	8.39	105.3	0.16	97	0.21	23.7
6.31	1.85	104.6	0.36	71	0.21	23.4
7.85	-1.99	99.2	0.07	19	0.11	21.0
-13.44	-9.35	97.2	0.20	37	0.11	20.2
-20.69	8.54	93.9	0.16	138	0.11	18.8
2.30	9.16	81.8	0.23	127	0.11	14.3
-4.95	7.17	86.0	0.23	87	0.11	15.8

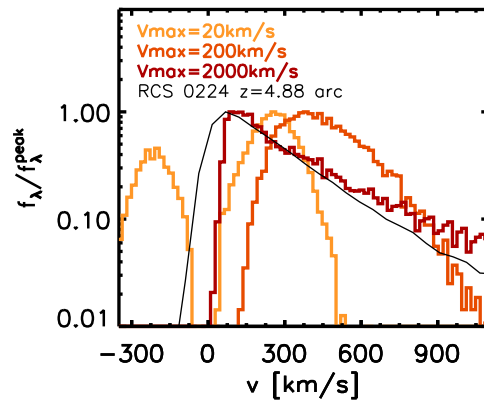
APPENDIX B: MEASURED PROPERTIES IN THE INDIVIDUAL LENSED IMAGES OF THE $z = 4.88$ ARC

In Section 3.2, we discussed the emission-lines properties of the $z = 4.88$ arc from the integrated spectrum over galaxy images 1, 2 and 3. In this appendix, we present the constraints that we can measure on the individual galaxy images. In Table B1, we give the redshift and EW measurements of the Ly α , C IV $\lambda 1548$ Å and C IV $\lambda 1551$ Å emission lines. The individual images (with the exception of galaxy image 1) are too faint to detect the weaker

Table B1. Detected spectral features of the $z = 4.88$ arc in the individual galaxy images.

Line	z	Δv (km s^{-1}) ^a	EW ₀ (Å)
Emission lines			
Ly $\alpha_{\text{im1}}^{\text{cont}}$	4.8770 ^b	68 ± 37	103 ± 21
Ly $\alpha_{\text{im2}}^{\text{cont}}$	4.8770 ^b	68 ± 37	141 ± 27
Ly $\alpha_{\text{im3}}^{\text{cont}}$	4.8770 ^b	68 ± 37	216 ± 167
Ly $\alpha_{\text{im4}}^{\text{cont}}$	4.8770 ^b	68 ± 37	126 ± 76
C IV $\lambda 1548$ Å _{im1}	4.8752	-23 ± 26	3.5 ± 0.3
C IV $\lambda 1548$ Å _{im2}	4.8750	-35 ± 27	8.8 ± 0.8
C IV $\lambda 1548$ Å _{im3}	4.8749	-39 ± 28	6.1 ± 1.4
C IV $\lambda 1551$ Å _{im1}	4.8756	-6 ± 26	2.5 ± 0.2
C IV $\lambda 1551$ Å _{im2}	4.8754	-15 ± 26	5.3 ± 0.5
C IV $\lambda 1551$ Å _{im3}	4.8757	-2 ± 28	3.9 ± 1.0

^aVelocity offset with respect to the systemic redshift $z_{[\text{O II}]} = 4.8757 \pm 0.0005$. Uncertainties combine the uncertainty on the line redshift with the uncertainty on the [O II] redshift. ^b Using the peak of the Ly α line.

**Figure B1.** The Ly α line profiles from Verhamme et al. (2006, see their fig. 7) assuming a velocity gradient $v \propto r$ in the outflowing gas, with three different maximum velocities (20, 200 and 2000 km s^{-1}), assuming a fixed column density of $2 \times 10^{20} \text{ cm}^{-2}$ and gas temperature of $T = 20000 \text{ K}$. The black line indicates the Ly α profile of the $z = 4.88$ arc presented in this work. The single Ly α peak, emerging close to the systemic velocity and the exponential slope to higher velocities is qualitatively well described by the Verhamme et al. (2006) high-velocity ($v_{\text{max}} = 2000 \text{ km s}^{-1}$) model.

emission lines or the absorption features, while galaxy image 4 is too faint to detect even the C IV lines at $>3.5\sigma$ and we therefore do not include these lines. We find that the Ly α lines peaks at the same pixel for every image, while the Ly α EW measurements are consistent with each other within the uncertainties. The C IV EWs are larger for image 2 and 3, which can be explained by the fact that these galaxy images are incomplete and the brightest star-forming region is not included in the measurement.

APPENDIX C: Ly α LINE PROFILES

In Section 3.2.2, we described the spectral line shape of the Ly α line observed in the $z = 4.88$ arc. The features of this line are well described by the model Verhamme et al. (2006) in which a smooth velocity gradient is present in the outflow of the galaxy. In this appendix, we present a comparison of the Verhamme et al. (2006) models for velocity gradients with different maximum outflow velocities (20, 200 and 2000 km s^{-1} , see their fig. 7) with the Ly α emission from the $z = 4.88$ arc in Fig. B1. We show spectra as a function of the velocity shift, converting from Doppler

units assuming a gas temperature $T = 20000$ K and column density of $2 \times 10^{20} \text{ cm}^{-2}$ as assumed in Verhamme et al. (2006), and we show the spectrum of the $z = 4.88$ arc with respect to $z_{[\text{O II}]} = 4.8757$. The main elements of the $\text{Ly}\alpha$ emission, such as the single peak emerging close to the systemic velocity and the exponential tail to higher velocities, are present in the model with a high (2000 km s^{-1}) maximum velocity and the strongest velocity gradient.

APPENDIX D: $\text{Ly}\alpha$ LINE-EMITTER CANDIDATES

In Section 4, we described our method and testing of a blind line-search for $\text{Ly}\alpha$ emitters at $z = 4.84\text{--}4.92$, $z = 5.64\text{--}5.80$ and $z = 6.54\text{--}6.65$. Here we present the *HST* and MUSE thumbnails of the individual sources and the one-dimensional spectrum from which the sources are identified in Figs D1, D2 and D3. We

also list the sources in Table D1. We detect asymmetric line profiles in all five sources at $z = 4.84\text{--}4.92$. However, measuring the continuum flux from the *HST* imaging using a fixed 0.5 arcsecond aperture centred on the $\text{Ly}\alpha$ detection, we find only one source (RCS0224_LAEz4p8773) detected at $>5\sigma$ in the I_{814} , J_{125} and H_{160} bands. A slightly weaker signal (4.6σ) is detected for RCS0224_LAEz4p8784 in the WFPC2 V_{606} band, while no significant detection ($<2\sigma$) is measured from the redder *HST* bands of the same source. If real, this flux belongs either to a foreground galaxy or else it would indicate that we have misidentified RCS0224_LAEz4p8784 as $\text{Ly}\alpha$ emission. However, the asymmetry of the line and the lack of secondary components in the spectrum favour the former interpretation. Furthermore, we find $\sim 3\sigma$ detections in the J_{125} band for two sources at $z \sim 5.7$, RCS0224_LAEz5p7405 and RCS0224_LAEz5p7360. For the 9 $\text{Ly}\alpha$ candidates at $z = 5.64\text{--}5.80$ and $z = 6.54\text{--}6.65$, we do not have enough S/N to detect the asymmetric profiles, nor do we detect the sources in the *HST* imaging at $>3.5\sigma$.

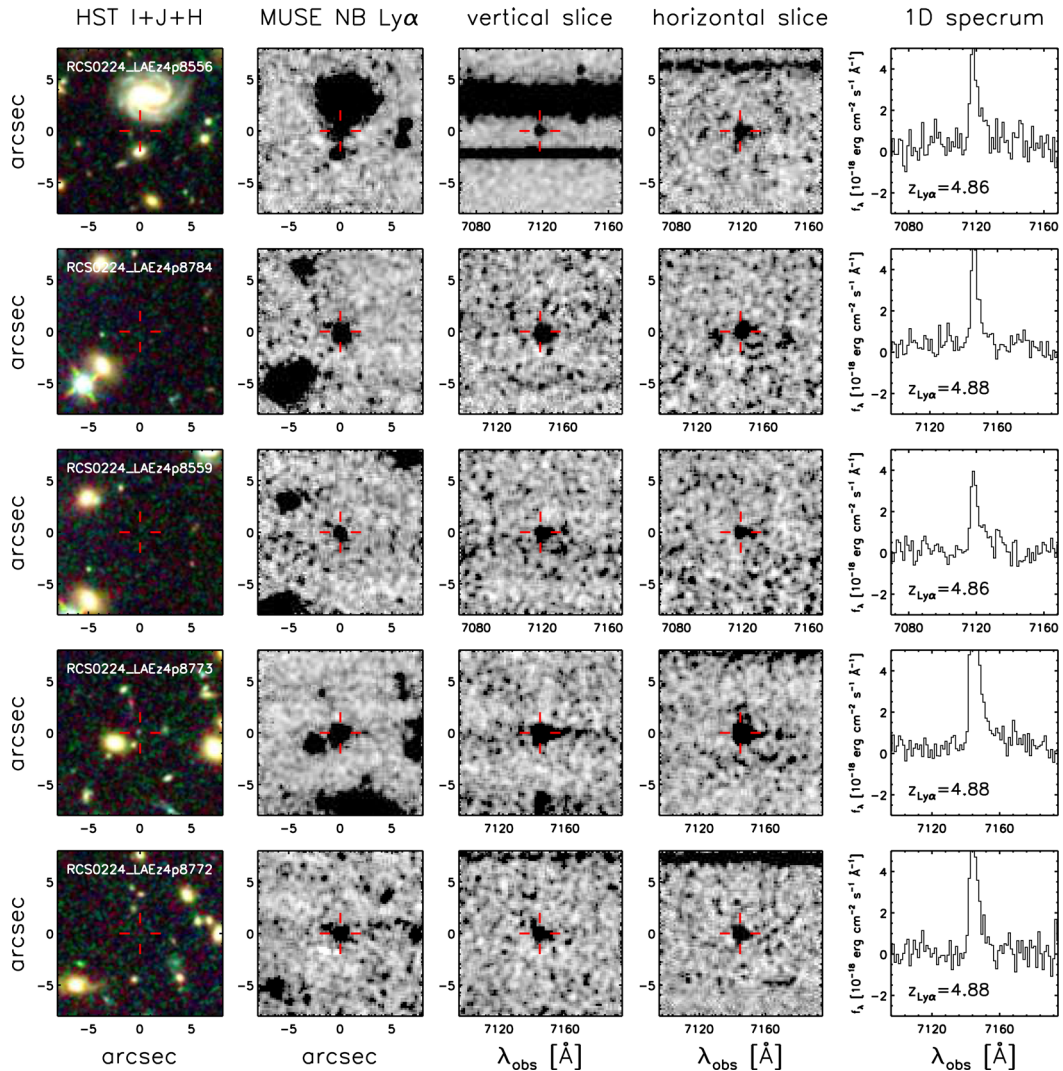


Figure D1. $\text{Ly}\alpha$ line-emitter candidates in the redshift range $z = 4.84\text{--}4.92$. From left to right, the panels show the combined *HST* WFPC $V_{606} + I_{814}$ bands (smoothed and rebinned to the MUSE resolution), a narrow band over the FWHM of the identified line in the MUSE cube, a vertical slice from the MUSE cube centred on the line, a horizontal slice of the cube centred on the line and the extracted one-dimensional spectrum from which the line is identified.

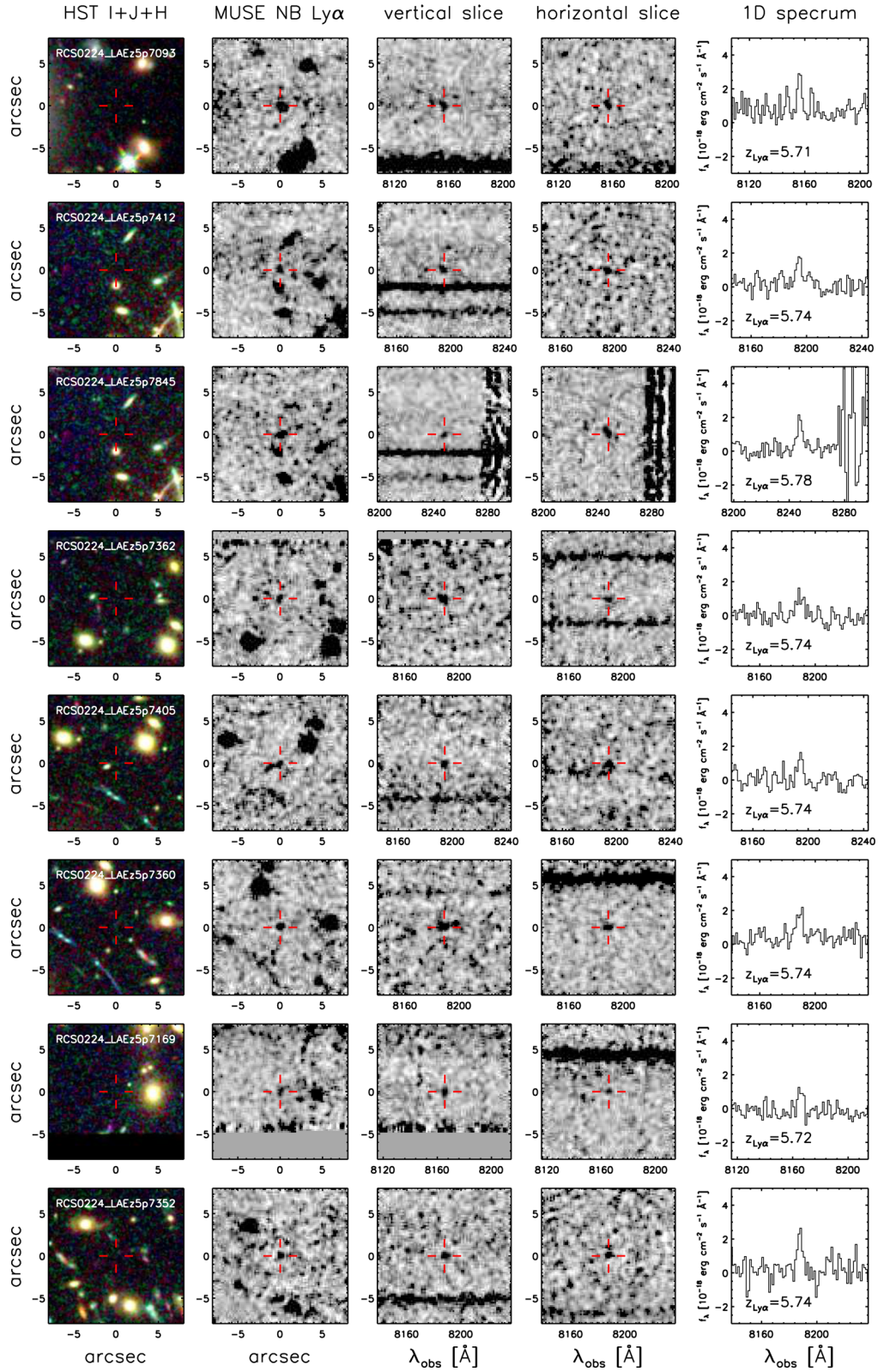


Figure D2. Ly α line-emitter candidates in the redshift range $z = 5.64\text{--}5.80$. Panels are as described in Fig. D1.

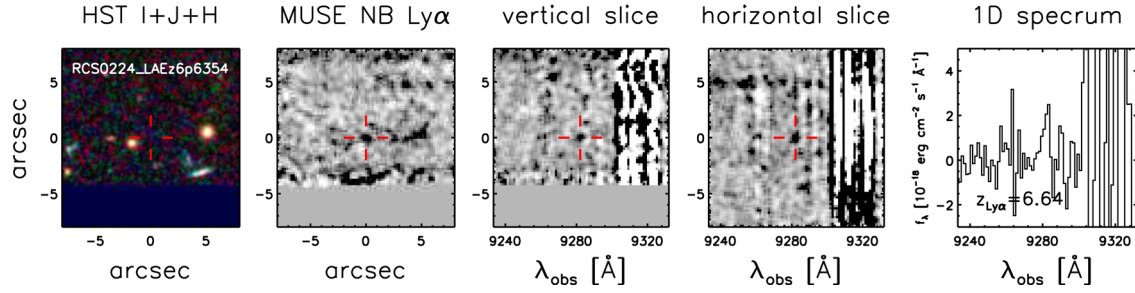


Figure D3. $\text{Ly}\alpha$ line-emitter candidate in the redshift range $z = 6.54\text{--}6.65$. Panels are as described in Fig. D1.

Table D1. $\text{Ly}\alpha$ emitter candidates.

ID (short ID ^a)	RA	Dec.	$z_{\text{Ly}\alpha}$
RCS0224_LAEz4p8556 (11)	02:24:36.38	−00:02:17.2	4.856
RCS0224_LAEz4p8784 ^b (12)	02:24:35.93	−00:02:51.2	4.878
RCS0224_LAEz4p8559 ^c (13)	02:24:35.83	−00:02:47.8	4.856
RCS0224_LAEz4p8773 (14)	02:24:34.06	−00:02:10.0	4.877
RCS0224_LAEz4p8772 (15)	02:24:32.61	−00:02:10.8	4.877
RCS0224_LAEz5p7093 (16)	02:24:36.39	−00:02:49.6	5.709
RCS0224_LAEz5p7412 (17)	02:24:35.07	−00:02:18.4	5.741
RCS0224_LAEz5p7845 (18)	02:24:35.07	−00:02:18.2	5.785
RCS0224_LAEz5p7362 (19)	02:24:33.98	−00:02:06.0	5.736
RCS0224_LAEz5p7405 (110)	02:24:33.81	−00:02:14.0	5.741
RCS0224_LAEz5p7360 (111)	02:24:33.42	−00:02:16.6	5.736
RCS0224_LAEz5p7169 (112)	02:24:33.19	−00:02:56.0	5.717
RCS0224_LAEz5p7352 (113)	02:24:32.78	−00:02:19.6	5.735
RCS0224_LAEz6p6354 (114)	02:24:35.22	−00:02:56.8	6.635

^aThe ID corresponding to the source positions indicated in Fig. 1. ^bWe measure a potential 4.6σ detection in the *HST*/WFPC2 V_{606} band imaging for this source. If associated with the line emission, this detection would indicate a low-redshift solution for the emission line. However, since the line is clearly asymmetric and no secondary components are detected in the spectrum, we assume that this flux is associated with a foreground object, or else, that the detected flux arises due to non-Gaussian noise at the edge of the detector. ^cWe measure a $>5\sigma$ detections in the I_{814} , J_{125} and H_{160} bands for this source, consistent with this source being an $\text{Ly}\alpha$ emitter at $z = 4.856$.

This paper has been typeset from a \LaTeX file prepared by the author.